

1 **TROPES/CrIS carbon monoxide profile validation with NOAA GML and ATom in situ**
2 **aircraft observations**

3
4 Helen M. Worden¹, Gene L. Francis¹, Susan S. Kulawik², Kevin W. Bowman³, Karen Cady-
5 Pereira⁴, Dejian Fu³, Jennifer D. Hegarty⁴, Valentin Kantchev³, Ming Luo³, Vivienne H. Payne³,
6 John R. Worden³, Róisín Commane³, Kathryn McKain^{6,7}

7
8 ¹Atmospheric Chemistry Observations and Modeling (ACOM), National Center for Atmospheric Research (NCAR),
9 Boulder, CO, USA

10 ²BAER Institute, 625 2nd Street, Suite 209, Petaluma, CA, USA

11 ³Jet Propulsion Laboratory / California Institute for Technology, Pasadena, CA, USA

12 ⁴Atmospheric and Environmental Research Inc., Lexington, MA, USA

13 ⁵Dept. of Earth and Environmental Sciences, Lamont-Doherty Earth Observatory, Columbia University, Palisades,
14 NY, USA

15 ⁶Cooperative Institute for Research in Environmental Sciences (CIRES), University of Colorado, Boulder, CO, USA

16 ⁷Global Monitoring Division (GMD), National Oceanic and Atmospheric Administration, Boulder, CO, USA

17
18 *Correspondence to:* Helen Worden (hmw@ucar.edu)

19
20
21 **Abstract.** The new single pixel TROPES (TROpospheric Ozone and its Precursors from Earth
22 System Sounding) profile retrievals of carbon monoxide (CO) from the Cross-track Infrared
23 Sounder (CrIS) are evaluated using vertical profiles of in situ observations from the National
24 Oceanic and Atmospheric Administration (NOAA) Global Monitoring Laboratory (GML)
25 aircraft program and from the Atmospheric Tomography Mission (ATom) campaigns. The
26 TROPES optimal estimation retrievals are produced using the MUSES (MULTi-SpECTra, MULTI-
27 SpECies, MULTI-Sensors) algorithm which has heritage from retrieval algorithms developed for
28 the EOS/Aura Tropospheric Emission Spectrometer (TES). TROPES products provide retrieval
29 diagnostics and error covariance matrices that propagate instrument noise as well as the
30 uncertainties from sequential retrievals of parameters such as temperature and water vapor that
31 are required to estimate the carbon monoxide profiles. The validation approach used here
32 evaluates biases in column and profile values and the validity of the retrieval error estimates
33 using the mean and variance of the compared satellite and aircraft observations. CrIS-NOAA
34 GML comparisons had biases of 0.6 % for partial column average volume mixing ratios (VMR)
35 and (2.3, 0.9, -4.5) % for VMR at (750, 511, 287) hPa vertical levels, respectively, with standard
36 deviations from 9 % to 14 %. CrIS-ATom comparisons had biases of -0.04 % for partial column
37 and (2.2, 0.5, -3.0) % for (750, 511, 287) hPa vertical levels, respectively, with standard
38 deviations from 6 % to 10 %. The reported observational errors for TROPES/CrIS CO profiles
39 have the expected behavior with respect to the vertical pattern in standard deviation of the
40 comparisons. These comparison results give us confidence in the use of TROPES/CrIS CO
41 profiles and error characterization for continuing the multi decadal record of satellite CO
42 observations.

Deleted:

Deleted:

51 **1. Introduction**

52 Carbon monoxide (CO) is a useful tracer of atmospheric pollution with direct emissions from
53 incomplete combustion such as biomass and fossil fuel burning and secondary production from
54 the oxidation of methane (CH₄) and volatile organic compounds (VOC). Atmospheric CO
55 distributions have a seasonal cycle that is mainly driven by photochemical destruction, which
56 allows CO to build up over winter and early spring in higher latitudes. The lifetime of CO, weeks
57 to months, (e.g., Holloway et al., 2000), is long enough to allow observations of pollution plumes
58 and their subsequent long range transport, but short enough to distinguish the plumes against
59 background seasonal distributions (e.g., Edwards et al., 2004, 2006; Hegarty et al., 2009, 2010).
60 As a dominant sink for the hydroxyl radical (OH), CO plays a critical role in atmospheric
61 reactivity (e.g., Lelieveld et al., 2016) and is considered a short-lived climate pollutant (SLCP)
62 because of its impacts to methane lifetime and carbon dioxide and ozone formation (e.g., Myhre
63 et al., 2014; Gaubert et al., 2017).

64
65 Global observations of tropospheric CO from satellites started in 2000 with the NASA Earth
66 Observing System (EOS) Measurement of Pollution in the Troposphere (MOPITT) instrument
67 on Terra (Drummond et al., 2010), followed by the EOS Atmospheric Infrared Spectrometer
68 (AIRS, McMillan et al., 2005) on Aqua launched in 2002, the Scanning Imaging Absorption
69 Spectrometer for Atmospheric Chartography (SCIAMACHY, de Laat et al., 2006) on Envisat
70 launched in 2002, the EOS Tropospheric Emission Spectrometer (TES, Beer et al., 2006) on
71 Aura launched in 2004, the Infrared Atmospheric Sounding Interferometer (IASI, Clerbaux et al.,
72 2009) on the MetOp series beginning in 2006, the Cross-track Infrared Sounder (CrIS,
73 Gambacorta et al., 2014) on the Suomi National Polar-orbiting Partnership (SNPP) satellite
74 launched in 2011, and most recently the Joint Polar Satellite System (JPSS) series, TROPOMI on
75 the Sentinel-5 precursor in 2017, (Borsdorff, et al., 2018) and the Fourier Transform
76 Spectrometer (FTS-2) on the Greenhouse gases Observing SATellite-2 (GOSAT-2, Suto et al.,
77 2021), launched in 2018. Satellite CO observations are assimilated for reanalyses and operational
78 air quality forecasting (e.g., Gaubert, 2016; Inness et al., 2019; Miyazaki et al., 2020) and have
79 been used in inverse modelling analyses to estimate emissions and attribute sources for co-
80 emitted species such as CO₂ (e.g., Kopacz et al., 2010; Jiang et al 2017; Liu et al., 2017; Zheng
81 et al., 2019; Gaubert et al., 2020; Byrne et al., 2021; Qu et al., 2022). Trend analyses of satellite
82 CO observations (e.g. Worden et al., 2013; Buchholz et al., 2021) show a general decline of
83 atmospheric CO over the satellite record globally and in most regions, but with a slowing of this
84 decrease in recent years that emphasizes the need for continued satellite CO observations that are
85 validated and have reliable error characterization.

86 In this study, we evaluate the biases and reported uncertainties of single field of view (FOV) CO
87 retrievals, from the Cross-track Infrared Sounder (CrIS) onboard the SNPP satellite launched in
88 October, 2011. CrIS is a Fourier Transform Spectrometer (FTS) that has continuation
89 instruments on the current and planned JPSS series with JPSS1/NOAA-20 launched in 2017 and
90 planned launches in 2022, 2028 and 2032 (jpss.noaa.gov). The CrIS CO retrievals evaluated here
91 use the MUSES (MUlti-SpEctra, MUlti-SpEcies, MUlti-Sensors) algorithm (Fu et al., 2016,
92 2018, 2019) and are processed with the TROPRESS (Tropospheric Ozone and its Precursors from
93 Earth System Sounding) Science Data Processing System (Bowman et al., 2021). TROPRESS is a
94 NASA project that provides a framework for consistent data processing of ozone and ozone
95 precursors across different satellite instruments. TROPRESS retrievals use single FOV radiances

Deleted: Similar to the recent validation study for the MUSES single pixel CO retrievals from the Aura Atmospheric Infrared Sounder (AIRS) of Hegarty et al., (2022),...

Deleted: here

Deleted: the TROPRESS/MUSES

Deleted: (Bowman et al., 2021) from the Cross-track Infrared Sounder (CrIS) onboard the SNPP satellite launched in October, 2011.

Deleted: TROPRESS

Deleted: products

Deleted: (MUlti-SpEctra, MUlti-SpEcies, MUlti-Sensors)

Deleted: algorithm

Deleted: (Fu et al., 2016, 2018, 2019) with

Deleted: field of view (FOV)

111 in sequential optimal estimation [retrievals](#) (Rodgers, 2000) of temperature, water vapor, effective
112 cloud parameters, [ozone, CO and other trace gases](#), [allowing for full characterization of the](#)
113 [vertical retrieval sensitivity with an averaging kernel and error covariance](#) (Bowman et al.,
114 [2006](#)). TROPES/CrIS CO products differ from other available CrIS CO data products that
115 [combine 9 FOVs to obtain a single cloud-cleared radiance and corresponding retrieval of](#)
116 [atmospheric parameters such as the NOAA Unique Combined Atmospheric Processing System](#)
117 [\(NUCAPS\) \(Gambacorta et al., 2014, 2017; Nalli et al., 2020\) and the Community Long-term](#)
118 [Infrared Microwave Combined Atmospheric Product System \(CLIMCAPS\) \(Smith and Barnet,](#)
119 [2020\)](#).

120 TROPES data products report a separate matrix for the observational error terms along with the
121 total retrieval error covariance that includes the contribution of smoothing error. This is
122 important for evaluation of retrieval errors using in situ profiles since the validation comparison
123 removes the effect of smoothing in the retrieval by applying the retrieval averaging kernel and a
124 priori to the in situ profile before differencing (Rodgers and Connor, 2003). Similar comparisons
125 were performed in the recent validation study for the MUSES single FOV CO retrievals from the
126 Aura Atmospheric Infrared Sounder (AIRS) of Hegarty et al. (2022).

127 [Section 2 describes the TROPES retrievals and CO data products in more detail, and Section 3](#)
128 [describes the validation in situ data from the National Oceanic and Atmospheric Administration](#)
129 [\(NOAA\) Global Monitoring Laboratory \(GML\) aircraft network and the Atmospheric](#)
130 [Tomography Mission \(ATom\) campaigns](#). The validation methods are presented in Section 4 and
131 results are shown in Section 5 with a summary and conclusions in Section 6.

132

133 2. TROPES/CrIS single field of view CO profile retrievals

134 The first Cross-track Infrared Sounder (CrIS) was launched 28 October, 2011 on the SNPP
135 satellite into a sun-synchronous polar orbit with an altitude near 830 km, and an equator-crossing
136 time (ascending node) near 13:30 LT. CrIS is a Fourier Transform Spectrometer (FTS) operating
137 in three spectral bands between 648 cm^{-1} and 2555 cm^{-1} . This includes the R-branch of the
138 thermal infrared (TIR) CO (0-1) fundamental band above 2155 cm^{-1} . After launch, spectral
139 radiance data that included the CO band were collected using a spectral resolution of 2.5 cm^{-1} .
140 This resolution was relatively coarse and significantly limited the vertical sensitivity of CO
141 retrievals (Gambacorta et al., 2014). Following the decision to collect data at full-spectral
142 resolution ($\delta = 0.625 \text{ cm}^{-1}$), these finer resolution spectral radiances have been available since 4
143 December 2014. Here we only [utilize](#) the full-spectral resolution CrIS data.

144

145 2.1 TROPES retrieval approach

146 TROPES data processing (Bowman et al., 2021) produces retrievals of temperature, water
147 vapor and trace gases such as ozone (O_3), methane (CH_4), carbon monoxide (CO), ammonia
148 (NH_3) and peroxyacetyl nitrate (PAN) from single and multiple instruments including AIRS and
149 OMI, CrIS and TROPOMI. [The MUSES retrieval algorithm used in TROPES was developed](#)
150 [with heritage from Aura/TES retrieval processing](#). Bowman et al. (2021) describe the sequential
151 MUSES retrievals of temperature, water vapor and effective cloud properties for each FOV that
152 are necessary for the retrieval of CO. Each step in the sequence includes an iterative retrieval
153 with a forward model and updated estimate of the state vector of atmospheric parameters
154 following the *maximum a posteriori* (MAP) method. The forward model for radiative transfer at

Deleted: retrievals

Deleted: and CO

Deleted: .

Deleted: TROPES CrIS CO products differ from other available CrIS CO products that combine 9 FOVs to obtain a single cloud-cleared radiance and corresponding retrieval of atmospheric parameters such as the NOAA Unique Combined Atmospheric Processing System (NUCAPS) (Gambacorta et al., 2014, 2017) and the Community Long-term Infrared Microwave Combined Atmospheric Product System (CLIMCAPS) (Smith and Barnet, 2020).

Deleted: The MUSES algorithm was developed with heritage from Aura/TES retrieval processing and allows for full characterization of the vertical retrieval sensitivity with an averaging kernel and error covariance (Bowman et al., 2006). The TROPES/MUSES data products report a separate matrix for the observational error terms along with the total retrieval error covariance that includes the contribution of smoothing error. This is important for evaluation of retrieval errors using in situ profiles since the validation comparison removes the effect of smoothing in the retrieval by applying the retrieval averaging kernel and a priori to the in situ profile before differencing (Rodgers and Connor, 2003). The

Deleted: are described

Deleted: in Section 2

Deleted: are described in Section 3

Deleted:

Deleted: consider

Deleted: Here we consider the SNPP/CrIS-only TIR CO retrievals that use the \uparrow 2181-2200 cm^{-1} spectral range.

Deleted: .

188 CrIS TIR wavelengths uses Optimal Spectral Sampling (OSS, Moncet et al., 2015), which
189 includes effective cloud optical depth and height parameters (Eldering et al., 2008; Kulawik et
190 al., 2006).

191 Here we analyze TROPES/CrIS TIR-only CO retrievals that use the 2181-2200 cm^{-1} spectral
192 range. A priori profiles for TROPES CO retrievals are taken from the model climatology used
193 in Aura/TES processing (MOZART, Brasseur et al., 1998), with monthly variation over a 30°
194 latitude and 60° longitude grid. The a priori uncertainty covariance matrix used to constrain the
195 retrieval is the same as used for MOPITT profiles (Deeter et al., 2010) with 30 % uncertainty for
196 vertical CO parameters at all levels and correlation lengths corresponding to 100 hPa between
197 them in the troposphere.

198 The TROPES CO products have quality flags for screening cases that did not converge or that
199 have unphysical results. This screening checks the magnitude and spectral structure of radiance
200 residuals, cloud retrieval characteristics, and deviation of surface emissivity from a priori
201 values. Specifically, retrievals with good data quality of 1 have: radiance residual standard
202 deviation less than 12 times the radiance error, an absolute value of the radiance residual mean
203 less than 0.7 times the radiance error, $K \cdot \text{DL}$ (the normalized dot product of the Jacobians and
204 the radiance residual) less than 0.8, $L \cdot \text{DL}$ (the normalized dot product of the radiance and the
205 residual) less than 0.6, cloud top pressures below 90 hPa, mean cloud optical depths less than 50,
206 cloud variability (variation with respect to wavenumber) less than 3, and mean surface emissivity
207 that did not change by more than 0.06. These threshold values are based on comparisons with in
208 situ data and other satellite data to determine when retrievals are valid.

2.2 TROPES/CrIS CO data examples

210 Figure 1 shows an example of TROPES/CrIS CO data for 12 September 2020 when there were
211 significant fires in the western US. These retrievals are from a special data collection that
212 processed scenes selected from 0.25° x 0.25° latitude/longitude sub-sampling to enable
213 throughput with the available computing capacity (Bowman et al., 2021). The data in this
214 collection are pre-filtered for quality (see Section 2.1) and Fig. 1a shows all available day and
215 night retrievals. Fig. 1b shows the data after higher cloudy scenes are removed (i.e. cloud tops
216 with pressure < 700 hPa and cloud effective optical depth > 0.1). For reference, Fig. 1c shows
217 the mid-tropospheric average CO volume mixing ratio (VMR) for the a priori profiles used in the
218 retrievals and Fig. 1d shows a NASA Worldview (worldview.earthdata.nasa.gov) image from
219 SNPP/VIIRS (Visible Infrared Imaging Radiometer Suite) with clouds and smoke shown in true
220 color and red areas indicating fire and thermal anomalies. Since vertical profile retrievals using
221 TIR radiances have sensitivity to CO mainly in the free troposphere, Fig. 1 shows individual
222 retrievals with average VMR from vertical layers between 700 to 350 hPa. When all scenes are
223 included, the average degrees of freedom for signal (DFS) is 0.99 for the CrIS CO observations
224 in Fig. 1a, and when cloudy scenes are removed (Fig. 1b), the average DFS is 1.14 for the
225 remaining CrIS observations.

Formatted: Font: (Default) Times New Roman

Formatted: Font: (Default) Times New Roman

Formatted: Font: (Default) Times New Roman

Formatted: Font: (Default) Times New Roman

Formatted: Font: (Default) Times New Roman

Formatted: Font: (Default) Times New Roman

Formatted: Font: (Default) Times New Roman

Formatted: Font: (Default) Times New Roman

Formatted: Font: (Default) Times New Roman

Formatted: Font: (Default) Times New Roman

Formatted: Font: (Default) Times New Roman

Formatted: Font: (Default) Times New Roman

Formatted: Font: (Default) Times New Roman

Formatted: Font: (Default) Times New Roman

Formatted: Font: (Default) Times New Roman

Formatted: Font: (Default) Times New Roman

Formatted: Font: (Default) Times New Roman

Formatted: Font: (Default) Times New Roman

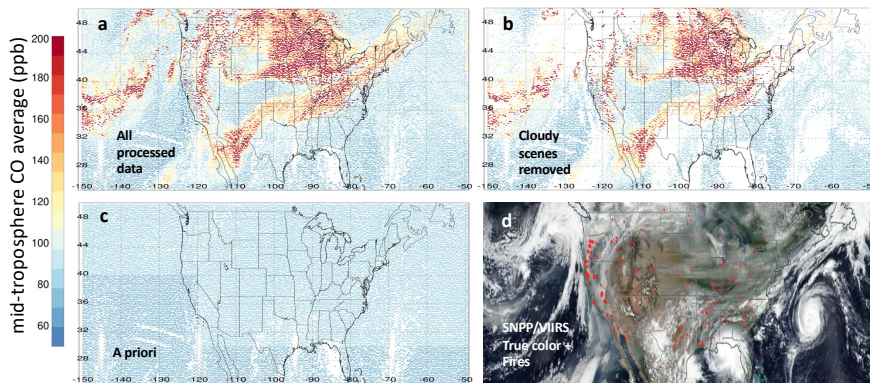
Formatted: Font: (Default) Times New Roman

Deleted:

Formatted: Font: (Default) Arial

Deleted: ,

Deleted: in Fig. 1b.

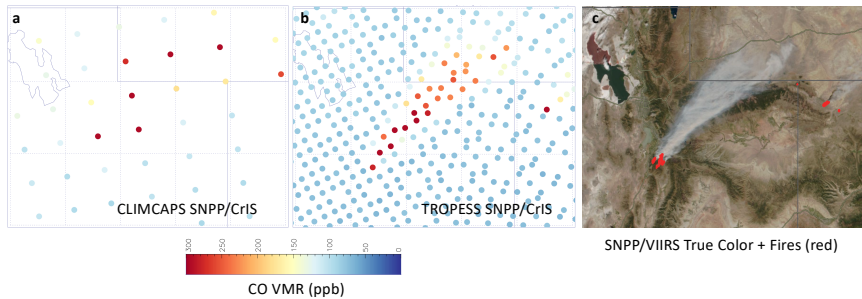


231
 232 **Figure 1.** *SNPP TROPES/CrIS and SNPP/VIIRS observations for 14 September, 2020. Panel*
 233 *(a) shows the average CO VMR for 700 to 350 hPa for all processed TROPES CO retrievals*
 234 *with good data quality (see text). Panel (b) shows the same free troposphere CO averages as (a)*
 235 *but with cloudy scenes removed (see text). Panel (c) shows the average TROPES a priori CO*
 236 *VMR for 700 to 350 hPa. Panel (d) shows the NASA Worldview SNPP/VIIRS image for 14*
 237 *September, 2020 with clouds and smoke (true color) and fire thermal anomalies (red).*

238
 239 As stated in the introduction, the TROPES single FOV products are different from the
 240 NUCAPS and CLIMCAPS products that combine 9 FOVs in a retrieval from a single cloud-
 241 cleared radiance (Susskind et al., 2003). These multiple FOV products have the advantage of
 242 increased global coverage in the presence of partially cloudy scenes but with coarser spatial
 243 resolution. Figure 2 shows an example of [SNPP CLIMCAPS](#) (Barnet, 2019) compared to [SNPP](#)
 244 [TROPES/CrIS CO products](#) (daytime only) on 13 September 2018 over the Pole Creek Fire in
 245 Utah. For CLIMCAPS, trace gas products with less than 1 DFS report mass mixing ratio (MMR)
 246 on a single level at the retrieval pressure with peak sensitivity, which is 500 hPa for CO. We
 247 converted MMR to VMR for Figure 2. This is compared to the tropospheric column average
 248 VMR from TROPES, so the background VMR values are close, but do not represent the same
 249 retrieved quantities. CrIS retrieval center locations are shown by the circles in Fig 2a, 2b, which
 250 are not intended to represent the spatial extent of the observations. The CLIMCAPS retrievals
 251 show elevated CO from the fire, but these combined FOV retrievals would give an overestimate
 252 of the plume width and do not distinguish the larger plume from the smaller fires to the east in
 253 Colorado.

Deleted: SNPP

Deleted: for SNPP



256
 257 **Figure 2.** *SNPP Observations of the Pole Creek Fire in Utah, USA, 13 September, 2018. The*
 258 *Great Salt Lake is in the upper left of each panel and state borders with Idaho, Wyoming and*
 259 *Colorado are indicated by solid straight lines. Dotted lines indicate a 1° latitude by 1° longitude*
 260 *grid, with top/left corner at 42°N, -113°E. Panel (a) shows CLIMCAPS/CrIS CO at 500 hPa*
 261 *(MMR converted to VMR). Panel (b) shows the TROPES/CrIS tropospheric CO column*
 262 *average VMR and panel (c) shows the corresponding NASA Worldview SNPP/VIIRS image with*
 263 *clouds and smoke (true color) and fire thermal anomalies (red).*

Formatted: Font: Not Bold

264 We note that retrievals of CO in the presence of smoke are not significantly affected by
 265 scattering for infrared observations at wavelengths $\lambda \sim 4.6 \mu\text{m}$, such as in the CrIS CO band.
 266 This is because Rayleigh scattering, which decreases by $1/\lambda^4$, is completely negligible and Mie
 267 scattering would be significant only for particles larger than $\sim \lambda/\pi = 1.5 \mu\text{m}$, (e.g., Seinfeld and
 268 Pandis, 1998), while the size distribution for biomass burning smoke particles peaks around 0.3
 269 μm (e.g., Reid et al., 2005). For the same Pole Creek fire in Fig. 2, Juncosa Calahorrano et al.,
 270 (2021) showed how SNPP/CrIS single pixel MUSES retrievals of acyl peroxy nitrates, also
 271 known as PAN, along with CO, can be used to follow fire plume chemical evolution. After
 272 subtracting background amounts, the normalized excess mixing ratios (NEMR) of PAN with
 273 respect to CO, computed from the CrIS observations for this plume, were consistent with in situ
 274 aircraft observations of smoke plumes from the summer 2018 WE-CAN (Western Wildfire
 275 Experiment for Cloud Chemistry, Aerosol Absorption, and Nitrogen) campaign.

Deleted: ,

276 3. Aircraft Data

277 3.1 NOAA GML aircraft network

278 Spanning 3 decades, NOAA GML aircraft network vertical profile observations are taken on
 279 semi-regular flights (~1/month) at fixed sites mostly in North America except for one site in
 280 Rarotonga, Cook Islands (Sweeney et al., 2015). These flights collect air samples using an
 281 automated flask system to obtain vertical profiles for each trace gas measured, from near the
 282 surface to around 400 hPa, depending on aircraft limitations at each site. Flask samples are then
 283 sent for laboratory analysis of a multitude of trace gases including CO, which was measured with
 284 vacuum UV-fluorescence spectroscopy during the time period of this analysis. CO mixing ratios
 285 are reported relative to the WMO X2014A scale (https://gml.noaa.gov/ccl/co_scale.html) and
 286 have reproducibility ~1 ppb (Sweeney et al., 2015). NOAA GML aircraft profiles of CO have
 287 been used for the long-term validation of the MOPITT CO record, with updated validation for
 288 each new data version (Deeter et al., 2019 and references therein). For the current analysis, we

290 use NOAA GML aircraft network observations of CO collected during 2016 and 2017 from 7
 291 locations (Table 1).

292 **3.2 ATom aircraft campaigns**

293 The Atmospheric Tomography Mission (ATom) was designed to study the most remote regions
 294 of the Pacific and Atlantic ocean air masses in each season (Thompson et al., 2022), which also
 295 makes the data valuable for validating satellite CO observations over a range of latitudes, with
 296 mostly background CO concentrations, except for where transported pollution plumes were
 297 encountered (Deeter et al., 2019; 2022; Martínez-Alonso et al., 2020; Hegarty et al., 2022). We
 298 use CO profiles from the quantum cascade laser spectrometer (QCLS) on the ATom campaigns
 299 1-4 (see Table 1). These NASA DC-8 flights obtained vertical profiles from 0.2 to 12 km altitude
 300 (~290 hPa) by ascending or descending approximately every 220 km. CO was measured at 1 Hz
 301 with QCLS reproducibility around 0.15 ppbv (McManus et al., 2010, Santoni et al., 2014). The
 302 QCLS data were calibrated to the X2014A CO WMO scale maintained by the NOAA GML.
 303

304
 305 Table 1. Aircraft in situ validation observations used in this study.

NOAA/GML Network flask/UV spectrometer (± 1 ppb CO)			
Code/Site name	Latitude ($^{\circ}$ N)	Longitude ($^{\circ}$ W)	Dates available
RTA/Raratonga	-21.25	159.83	2000-2021
TGC/Offshore Corpus Christi, TX	27.73	96.86	2003-2021
CMA/Offshore Cape May, NJ	38.83	74.32	2005-2022
THD/Trinidad Head, CA	41.05	124.15	2003-2022
NHA/Offshore Portsmouth, NH	42.95	70.63	2003-2022
ESP/Estevan Pt., BC	49.38	128.54	2002-2021
ACG/Alaska Coast Guard	57.74	152.50	2009-2021
NASA/ATom QCLS (± 0.15 ppb CO)			
ATom 1-4 Pacific	75 to -65	150 to 70	July 2016, Jan. 2017, Sep. 2017, April 2018
ATom 1-4 Atlantic	-75 to 80	65 to 20	Aug. 2016, Feb. 2017, Oct. 2017, May 2018

306 <https://gml.noaa.gov/ccgg/aircraft/>
 307 <https://espo.nasa.gov/atom/content/ATom>

308
 309 **4. Validation Methodology**

310 **4.1 Data selection, coincidence criteria and vertical extension of aircraft profiles**

311 TROPES/CrIS CO profiles are selected for comparison if they have retrieval quality of 1 and
 312 effective cloud optical depth less than 0.1 to ensure non-cloudy CrIS observations. We then find
 313 all eligible CrIS and aircraft profile pairs within 9 hours and 50 km distance. This has been a
 314 standard coincidence distance criterion for several validation studies (e.g., Deeter et al., 2019;
 315 2022; Hegarty et al., 2022). Tang et al. (2020) found very little sensitivity in MOPITT CO
 316 validation results for 25, 50, 100 and 200 km coincidence except for the cases with a 25 km
 317 radius that resulted in an insufficient number of matches for meaningful statistics. The Tang et
 318 al. (2020) study also tested the time coincidence criterion (12, 6, 2 and 1 hour) with similar
 319

Deleted: E
 Deleted: -
 Deleted: -
 Deleted: -
 Deleted: -
 Deleted: -
 Deleted: -
 Deleted: -
 Deleted: -
 Deleted: -
 Deleted: -
 Deleted: -

Deleted:
 Deleted: ,

334 conclusions. Application of the 9 hour/ 50 km coincidence criteria yielded 2092 CrIS/aircraft
 335 profile pairs for NOAA GML flights from 2016 and 2017 and 1052 profile pairs for the ATom 1-
 336 4 campaigns. Since the aircraft profiles used for validation do not span the full vertical range of
 337 satellite retrieved profiles, we must extend these with a reasonable approximation of atmospheric
 338 CO to facilitate the comparison as described below in section 4.2. Here we use the TROPES
 339 a priori profiles (from model climatology, described above) to extend the in situ profiles above the
 340 highest altitude sampled. The a priori profile is scaled to match the CO abundance of the aircraft
 341 measurement at the highest altitude. The choice of model and approach for extending the aircraft
 342 profiles are examined more in Tang et al., (2020) and Hegarty et al. (2022), with similar
 343 conclusions that the impacts apply mostly to bias estimates in the middle to upper troposphere.
 344 Martínez-Alonso et al., (2022) compute the uncertainty introduced by this extension explicitly
 345 using NOAA AirCore in situ balloon profiles that sample into the stratosphere (Karion et al.,
 346 2010). This uncertainty is computed for validation using aircraft profiles (with top samples
 347 around 400 hPa for NOAA/GML) by comparing MOPITT profiles to truncated and extended
 348 AirCore profiles vs. the true full AirCore profiles. The comparison error introduced by the
 349 extension was at most 3 % around 300 hPa, and much less than the standard deviation of
 350 MOPITT and full AirCore profile differences (~7-10 %) in the upper troposphere. We also note
 351 that for ATom profiles, the highest altitude samples are normally taken around 12 km (~200 hPa)
 352 and the profile extension therefore has minimal impact on tropospheric validation results.

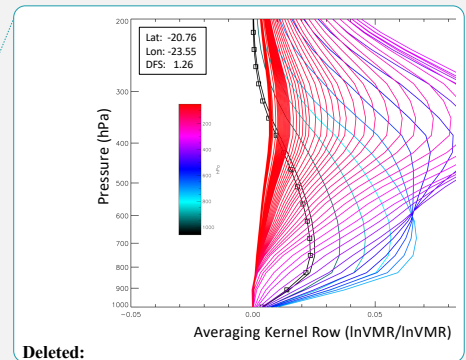
354 4.2 Comparison of TROPES satellite and aircraft observations

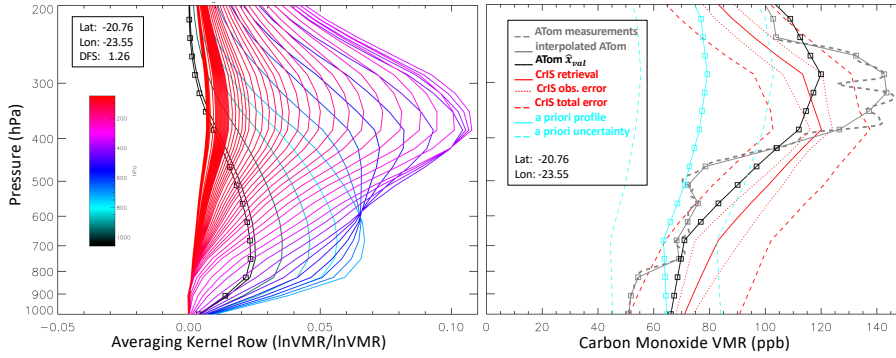
355 In order to account for the satellite observational and retrieval approach, including prior
 356 information, when comparing satellite retrieval products to in situ measurements of CO, we
 357 apply the instrument operator to convert the in situ profile into the values that would be retrieved
 358 for the same air mass assuming the satellite instrument and retrieval (Jones et al., 2003, Rodgers
 359 and Conner, 2003, Worden et al., 2007):

$$361 \mathbf{x}_{val} = \mathbf{x}_a + \mathbf{A}(\mathbf{x}_{val} - \mathbf{x}_a) \quad (1)$$

362 where \mathbf{x}_{val} is the aircraft or sonde in situ profile being used for validation (following extension,
 363 described above, and linear interpolation to the satellite vertical grid), \mathbf{x}_a is the a priori profile
 364 used in the TROPES retrieval, \mathbf{A} is the averaging kernel matrix that describes the observation
 365 and retrieval vertical sensitivity to the true state and \mathbf{x}_{val} is the in situ validation profile
 366 transformed by the satellite instrument operator. This operation accounts for both the broad
 367 vertical resolution (or “smoothing”) of remotely sensed measurements and the influence of the a
 368 priori, which is especially important in the vertical ranges where satellite observations have low
 369 sensitivity to CO abundance. Figure 3 shows an example of the averaging kernel \mathbf{A} and a
 370 validation comparison where Eq. 1 is applied to an ATom in situ profile.
 371
 372

Deleted: ,
 Deleted: ,
 Deleted: ,





Deleted: [redacted]

377
 378 **Figure 3.** Examples of TROPES/CrIS CO averaging kernel (A) (left panel) and the validation
 379 process (right panel). The colors of the averaging kernel indicate the pressure level (66 levels
 380 from 1017.45 to 0.1 hPa) corresponding to each row, with the surface level row also indicated
 381 by the squares. The degrees of freedom for signal (DFS), given by the sum of the diagonal (i.e.
 382 trace) of this averaging kernel is 1.26. The right panel shows the CrIS CO profile retrieval (solid
 383 red line) with total error (dashed red lines), observation error (dotted red lines), apriori profile
 384 (solid cyan line with squares) and diagonal uncertainty (dashed cyan lines). The closest ATom
 385 aircraft profile had 10.4 km; 3.5 hr coincidence. The original ATom profile (dashed grey line) is
 386 interpolated to the CrIS vertical grid (solid grey with squares) and transformed by the
 387 instrument operator to give ATom x_{val} (Eq. 1) (solid black line with squares).
 388

4.3 Evaluating TROPES CO reported observational errors

389 Following Bowman et al., (2006, 2021), for retrieved parameter x (e.g., CO abundance) with a
 390 priori covariance S_a , radiance measurement covariance S_e , Jacobian matrix $K = \frac{\partial L}{\partial x}$, for radiance
 391 $L(x)$, gain matrix $G = (K^T S_e^{-1} K + S_a^{-1})^{-1} K^T S_e^{-1}$ and averaging kernel $A = GK$, the a
 392 posteriori error covariance can be written as the sum of:
 393

$$394 \quad S_x = S_{smoothing} + S_{observational} \quad (2)$$

$$395 \quad \text{with } S_{smoothing} = (I - A_{xx}) S_a (I - A_{xx})^T \text{ and}$$

$$396 \quad S_{observational} = S_{noise} + S_{cross-state} + S_{systematic} \quad (3)$$

$$397 \quad \text{where } S_{noise} = G S_e G^T, \quad S_{cross-state} = \sum_{b_ret} A_{xs} S_a^{b_ret} A_{xs}^T \text{ and}$$

$$398 \quad S_{systematic} = \sum_b G K_b S_b (G K_b)^T \quad (4)$$

399 In this notation, b variables are parameters that are held constant in the CO retrieval (such as
 400 temperature and water vapor), but affect the radiance observation and are propagated through
 401 Jacobian K_b while b_ret variables are retrieved along with CO (such as surface emissivity) and
 402 have corresponding off-diagonal terms in the full retrieval averaging kernel matrix. When we
 403
 404

Deleted: used for the CO retrieval

411 apply the satellite instrument operator in Eq. 1 to the in situ aircraft profile, we are accounting
412 for the smoothing error term. Thus, we expect differences between x_{val} and our retrieved x to be
413 due to observational error terms (Eq. 3) and to geophysical differences from the sampling of
414 different airmasses and surface locations because of imperfect coincidence.

415 5. Validation Results

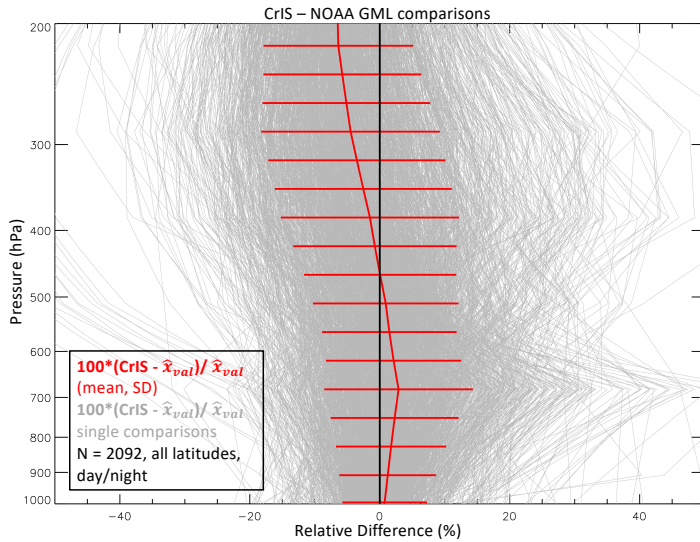
416 5.1 TROPES/CrIS CO comparisons with NOAA GML aircraft data

417 After extending the in situ profiles vertically (described in Sec. 4.1) and applying Eq. 1, we
418 compute the differences between satellite retrievals and transformed aircraft profiles. Figure 4
419 shows the bias (% relative difference) of the CrIS CO retrieved profiles with respect to NOAA
420 GML aircraft profiles (x_{val}). A similar pattern of positive bias in the lower to mid troposphere
421 and negative bias in the upper troposphere is observed for MUSES/AIRS profiles compared to
422 NOAA GML flights (Hegarty et al., 2022). However, MOPITT (version 9, TIR-only data)
423 comparisons to NOAA GML (Deeter et al., 2022) have almost the opposite vertical bias pattern
424 with a negative bias (-1.6 %) in the lower to middle troposphere and a positive bias (0.6 %) in
425 the upper troposphere. [Since TROPES and MOPITT retrievals both use optimal estimation
426 algorithms and a similar prior CO error covariance, this different vertical bias pattern is most
427 likely due to instrument differences. MOPITT uses gas filter correlation radiometry instead of
428 spectroscopy to detect CO absorption in the atmosphere with corresponding differences in
429 vertical sensitivity that are determined from gas cell pressure rather than spectral resolution.
430 After accounting for retrieval differences in a priori profiles and covariances between MOPITT
431 and IASI \(another FTS instrument\), George et al. \(2015\) find a similar positive bias for MOPITT
432 in the upper troposphere.](#)

433 Table 2 gives the mean bias and standard deviations for selected pressures and partial column
434 average VMR over different observing conditions (land, ocean, day and night). The partial
435 column refers to the CO column between the minimum and maximum flight altitudes of each
436 aircraft profile. The average VMR over this range is computed by interpolating both the CrIS
437 retrieval and the aircraft x_{val} profile to these endpoints. Since aircraft flights normally occur
438 during daytime, there are fewer coincident pairs for CrIS night retrievals. Tang et al. (2020) find
439 larger bias and variance for nighttime MOPITT data in comparisons with in situ aircraft data,
440 especially for flights over urban regions, suggesting more night validation flights are needed to
441 properly evaluate night satellite retrievals.

Deleted:

Deleted: -



448
449 **Figure 4.** Relative differences (%) in single CrIS retrievals with coincident NOAA GML x_{val}
450 profiles (grey) and the average % difference with 1σ horizontal bars (red). Both day and night
451 CrIS observations are included for coincidence search with 1866 day and 266 night comparison
452 pairs found.
453

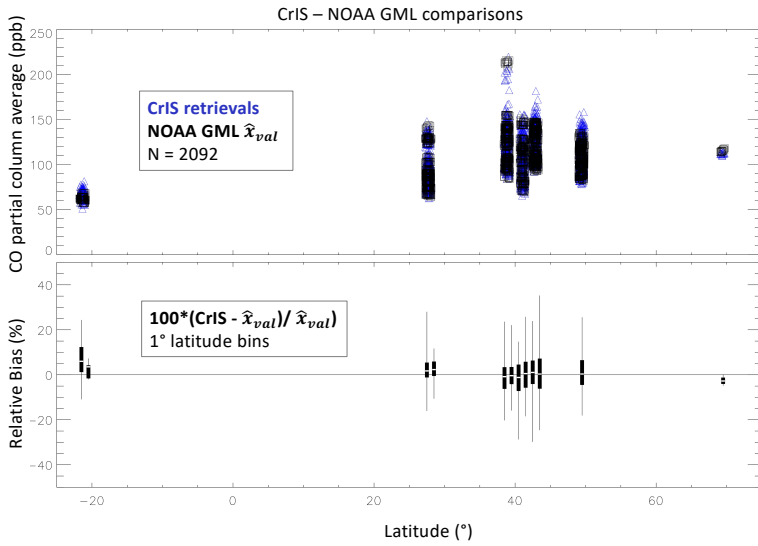
454 Table 2. Bias and standard deviation (SD) for comparisons of [SNPP TROPES/CrIS CO](#)
455 retrievals and in situ CO profiles from NOAA GML flights.

Obs. type	% bias 750 hPa	% SD 750 hPa	% bias 511 hPa	% SD 511 hPa	% bias 287 hPa	% SD 287 hPa	% bias Column	% SD Column	# pairs
All	2.29	9.84	0.92	11.20	-4.48	13.76	0.57	8.56	2092
Land	3.04	10.85	-0.044	11.95	-6.15	13.97	1.24	9.46	853
Ocn	1.78	9.04	1.58	10.59	-3.33	13.49	0.11	7.84	1239
Day	1.97	9.79	0.13	10.93	-5.37	13.32	0.23	8.77	1866
Ngt	4.94	9.86	7.36	11.27	2.81	15.05	3.41	5.82	266

456
457 Figure 5 shows how the observed partial column average VMR and CrIS retrieval bias with
458 respect to NOAA GML x_{val} profiles vary with latitude and Figure 6 shows how these vary with
459 time. No significant bias dependence on latitude is observed for the NOAA GML flight sites.
460 Although a bias drift of -0.007 ± 0.001 %/day is detected, we recognize that our comparison
461 time range is not sufficient for a reliable estimate of bias drift, and more years of comparisons
462 would be required.
463
464

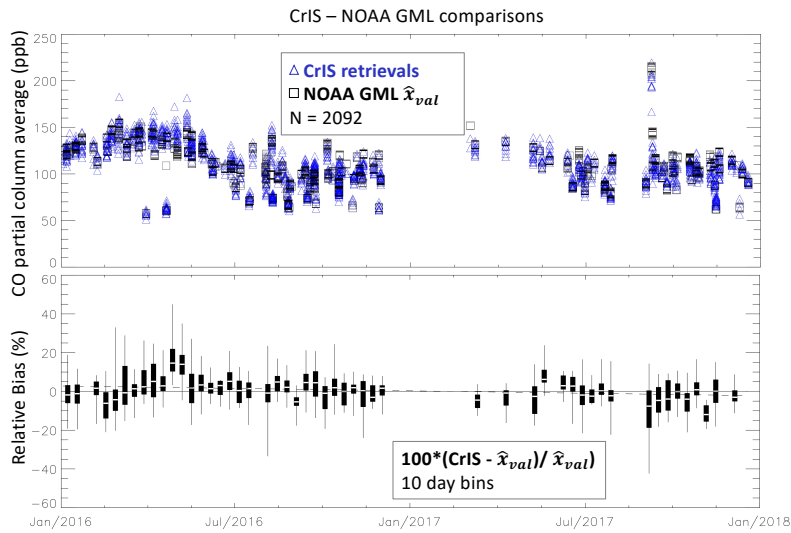
Deleted: SNPP

Formatted Table



466
467 **Figure 5.** Latitude dependence of CO partial column average VMR (ppb) for TROPES/CrIS
468 retrievals and NOAA GML \hat{x}_{val} (upper panel) and bias difference statistics (lower panel) shown
469 by box/whisker symbols representing minimum and maximum values (whisker), lower quartile
470 (box bottom), median (white stripe), and upper quartile (box top). A minimum of 5 comparisons
471 per bin was required.

Deleted:



472

474 **Figure 6.** Time dependence of CO partial column average VMR (ppb) for TROPES/CrIS
475 retrievals and NOAA GML x_{val} (upper panel) and bias difference statistics (lower panel) shown
476 by box/whisker symbols representing minimum and maximum values (whisker), lower quartile
477 (box bottom), median (white stripe), and upper quartile (box top). A minimum of 5 comparisons
478 per bin was required. The dashed line indicates a fit for bias drift (see text).

479 5.2 TROPES/CrIS CO validation with ATom

481 Figure 7 shows the bias (% relative difference) of the CrIS CO retrieved profiles with respect to
482 ATom x_{val} in situ profiles for all latitudes and 3 latitude ranges: 30°S to 30°N, 90°S to 30°S, and
483 30°N to 90°N. The vertical behavior of the bias is similar to the above CrIS comparisons with
484 NOAA GML flights, with positive bias in the lower troposphere and negative bias in the upper
485 troposphere and is also similar to the MUSES/AIRS CO profiles compared to ATom flights
486 (Hegarty et al., 2022). However, for MOPITT V9T comparisons to ATom flights (Deeter et al.,
487 2022), the vertical bias pattern is again mostly opposite, with a negative bias (~4 %) in the lower
488 to mid troposphere and a positive bias (~2 %) in the upper troposphere. [This TROPES/CrIS CO
489 bias also differs from Nalli et al. \(2020\) who examined the bias of NUCAPS profiles \(including
490 CO\) with respect to ATom in situ profiles. That study, using the multiple FOV NUCAPS
491 retrievals, found a small positive bias \(~2%\) for SNPP/CrIS CO with respect to ATom CO at all
492 tropospheric vertical levels after applying their averaging kernels.](#)

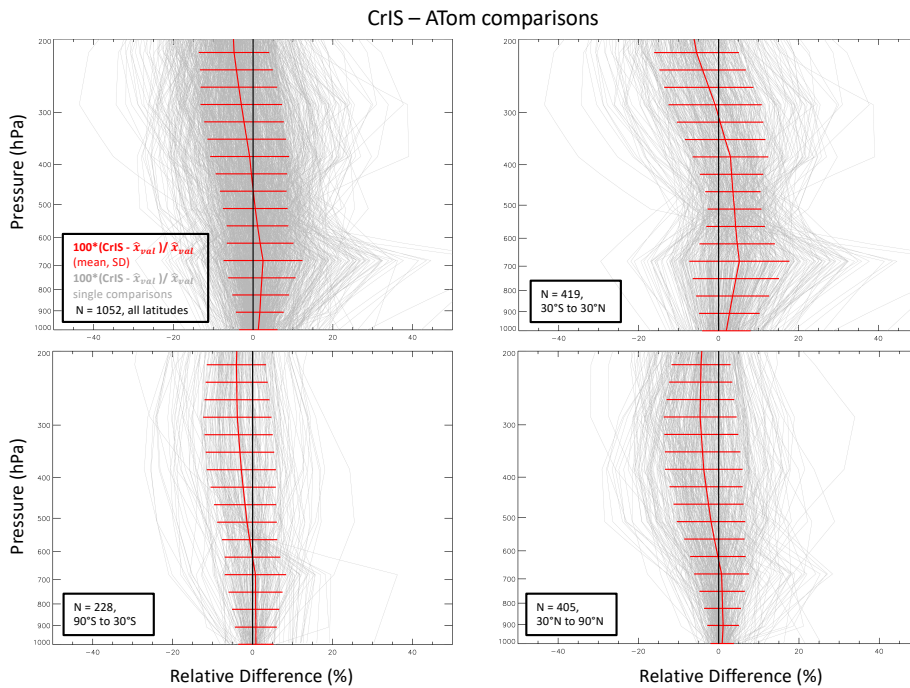
494 CrIS CO comparisons with ATom have less variance than comparisons with NOAA GML,
495 especially for 90°S to 30°S. Table 3 gives the mean bias and standard deviations for selected
496 pressures and partial column average VMR over different observing conditions (land, ocean, day
497 and night) and latitude ranges. As described above, the partial column average VMR is computed
498 over the altitude ranges of each aircraft profile. Due to the nature of the ATom campaign, there
499 are fewer observations over land.

Deleted:

Deleted:

Deleted: -

Deleted:



504
 505 **Figure 7.** Relative differences (%) in single CrIS retrievals with coincident ATom x_{val} profiles
 506 (grey) and the average % difference with 1σ horizontal bars (red). Latitude ranges are
 507 indicated in each panel along with the number of comparison pairs. Both day and night CrIS
 508 observations are included.

509
 510 Figure 8 shows how the observed partial column average VMRs and CrIS retrieval bias with
 511 respect to ATom x_{val} profiles vary with latitude. It appears that tropical and northern hemisphere
 512 sub-tropical latitude ranges have a slightly higher positive bias than what is observed for higher
 513 latitudes, potentially indicating a TROPES/CrIS retrieval issue with water vapor or some other
 514 interferent that is not fully characterized and requires further investigation. [For example, Deeter](#)
 515 [et al. \(2018\) found that an empirical correction to MOPITT radiances resulting from a linear](#)
 516 [dependence on water vapor removed most of the latitude dependent bias in MOPITT CO](#)
 517 [profiles. Another gas interferent in the TIR CO band is N₂O and we will also need to consider](#)
 518 [the latitude dependent N₂O anomalies observed by ATom \(Gonzalez et al., 2021\) when assessing](#)
 519 [the contributions to this latitude dependence in TROPES/CrIS CO bias.](#)

Deleted:

Formatted: Subscript

Formatted: Subscript

520
 521
 522
 523
 524

526
527

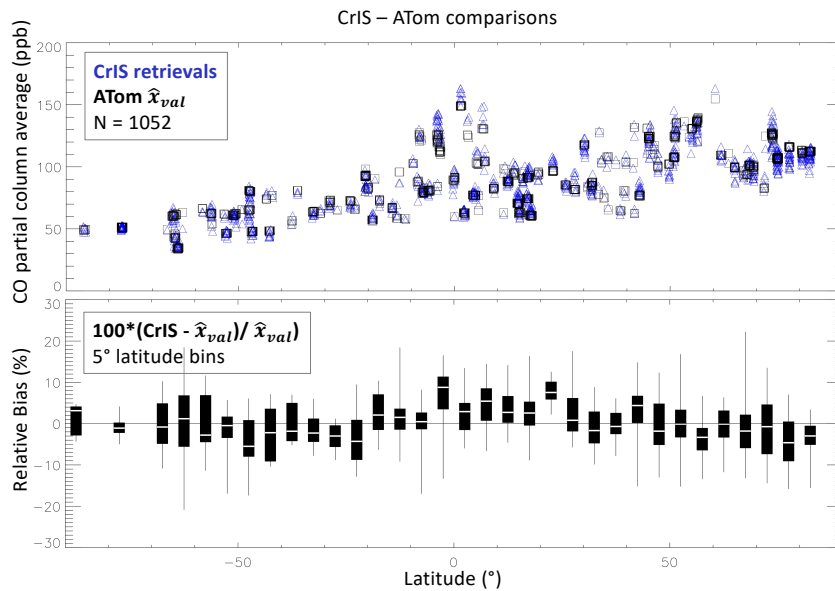
Table 3. Bias and standard deviation (SD) for comparisons of **SNPP** TROPES/CrIS CO retrievals and in situ CO profiles from ATom flight campaigns 1-4.

Obs. type	Latitude Range (°)	% bias 750 hPa	% SD 750 hPa	% bias 511 hPa	% SD 511 hPa	% bias 287 hPa	% SD 287 hPa	% bias Col.	% SD Col.	# pairs
All	all	2.21	8.46	0.54	8.12	-2.95	10.24	-0.035	5.91	1052
Land	all	1.20	4.15	-0.49	7.59	-2.95	10.46	-0.79	7.09	102
Land	30S-30N	-	-	-	-	-	-	-	-	1
Land	30N-90N	1.22	4.27	-0.69	7.76	-3.25	10.70	-0.91	7.32	95
Land	90S-30S	0.12	0.29	0.89	2.35	1.84	4.65	0.67	1.86	6
Ocn	all	2.32	8.79	0.65	8.17	-2.95	10.21	0.046	5.76	950
Ocn	30S-30N	4.32	10.80	3.96	6.75	-0.86	11.67	2.33	5.44	418
Ocn	30N-90N	0.75	6.01	-2.28	8.70	-5.03	8.51	-2.22	6.34	310
Ocn	90S-30S	0.74	6.85	-1.46	7.5	-3.98	8.57	-1.09	3.49	222
Day	all	2.62	8.76	0.53	7.91	-3.21	9.81	0.010	5.85	782
Day	30S-30N	4.94	11.42	3.55	6.57	-2.01	10.99	2.23	5.16	300
Day	30N-90N	0.91	5.76	-1.63	8.62	-4.33	9.22	-1.68	6.74	331
Day	90S-30S	1.79	6.90	-0.72	6.71	-3.11	8.12	-0.70	2.91	151
Ngt	all	1.03	7.39	0.57	8.71	-2.21	11.36	-0.17	6.08	270
Ngt	30S-30N	2.79	8.82	5.02	7.07	2.03	12.73	2.59	6.09	119
Ngt	30N-90N	0.68	5.15	-3.16	7.93	-5.88	8.45	-2.98	5.84	74
Ngt	90S-30S	-1.35	5.94	-2.73	8.58	-5.25	9.15	-1.73	4.30	77

528

Deleted: SNPP

Formatted Table



529
530

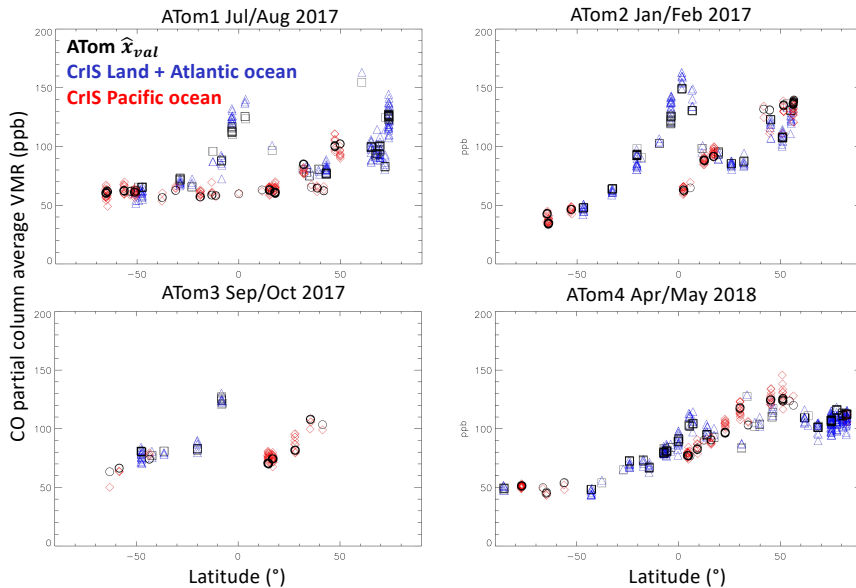
Figure 8. Latitude dependence of CO partial column average VMR (ppb) for TROPES/CrIS retrievals and ATom x_{val} (upper panel) and bias difference statistics (lower panel) shown by box/whisker symbols representing minimum and maximum values (whisker), lower quartile (box

Deleted:

536 bottom), median (white stripe), and upper quartile (box top). A minimum of 5 comparisons per
 537 bin was required.

538

539 In Figure 9, we examine the seasonal behavior of CO sampled by ATom and CrIS in mostly
 540 remote ocean regions. In the high latitude southern hemisphere (SH), we see the lowest values in
 541 summer and fall (Jan/Feb and Apr/May) as expected due to the chemical destruction of CO in a
 542 region with few local combustion sources. In the tropics, we find high values corresponding to
 543 African and South American biomass burning plumes over the Atlantic in all seasons except
 544 Northern Hemisphere (NH) spring. Lower values of CO in the tropics for NH summer and winter
 545 correspond to profiles over the Pacific ocean (e.g., Strode et al., 2018, Bourgeois et al., 2020).
 546 The close alignment of the CrIS and ATom x_{val} partial column average values in Fig. 9 indicates
 547 that CrIS is able to capture the seasonal, latitudinal and hemispherical variations observed by
 548 ATom.
 549



550

551 **Figure 9.** Latitude dependence of partial column average CO for each ATom campaign. Black
 552 squares ATom x_{val} partial column average values over Atlantic Ocean scenes; black circles
 553 indicate ATom values over Pacific Ocean scenes. Blue triangles indicate CrIS CO partial
 554 column average values over land and Atlantic Ocean scenes; red diamonds indicate CrIS values
 555 over Pacific Ocean scenes.
 556

557 **5.3 Dependence on CO amount**

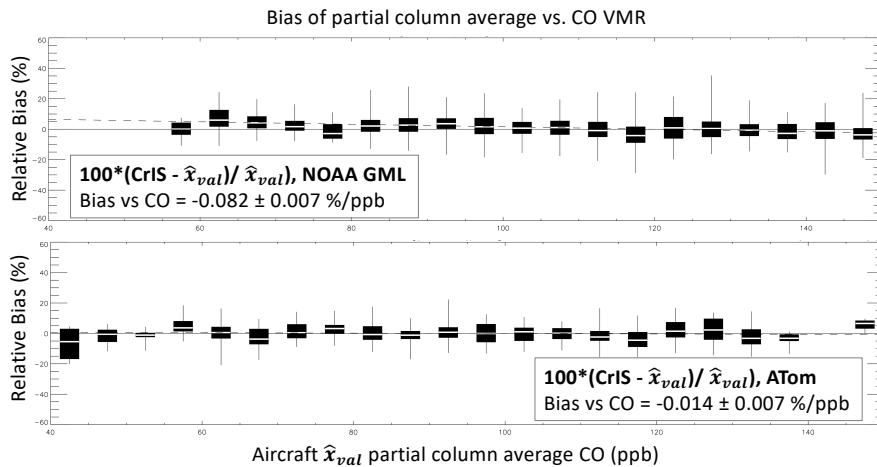
558 For both the NOAA GML and ATom flights we find a small negative dependence of
 559 TROPES/CrIS retrieval bias with respect to CO amount, with magnitude less than 0.1 %/ppb.

560 Figure 10 shows how the partial column average VMR bias varies with CO VMR for the two

Deleted:

562 validation data sources and we can also see how ATom flights sampled air with lower CO
 563 concentrations. Figure 10 indicates that TROPES/CrIS CO average column VMRs have very
 564 little dependence on CO amount and we find similar results for CrIS retrieved CO at vertical
 565 levels 511 hPa and 750 hPa (shown in the supplementary material).
 566

Deleted: .
 Deleted:



567
 568 **Figure 10.** Bias of CrIS partial column average CO vs CO amount for NOAA GML flights in top
 569 panel and ATom flights in bottom panel with box/whisker symbols in 5 ppb bins. Linear
 570 regression results are shown in the legend boxes.
 571

572 **5.4 Evaluation of TROPES/CrIS CO retrieval observational errors**

573 Here we compare the observed variance of differences between retrieved CrIS CO profiles and in
 574 situ aircraft profiles, after applying Eq. 1, with the TROPES reported observational errors
 575 defined in Eqs. 3 and 4. As described in section 4.3, we expect the differences between retrieved
 576 CrIS and aircraft CO profiles (x_{val}) to have a variance due to the combination of observational
 577 errors and geophysical variation from imperfect coincidence. Figure 11 shows comparisons of
 578 individual and average computed observational fractional errors to the standard deviation (SD) of
 579 CrIS x_{val} profile differences as well as the diagonal for the a priori covariance and the SD of
 580 prior x_{val} profile differences. As expected, the average observational errors are less than
 581 SD(CrIS x_{val}), but in some vertical ranges, they are much less and could be underestimated via
 582 instrument and systematic error assumptions in the TROPES retrieval as Hegarty et al. (2022)
 583 suggest. Additional studies to test the sensitivity of the comparison variance to a range of
 584 coincidence criteria are needed to confirm a retrieval underestimate, but these would require
 585 several repeated validation measurements for the same observing conditions.
 586

Deleted:

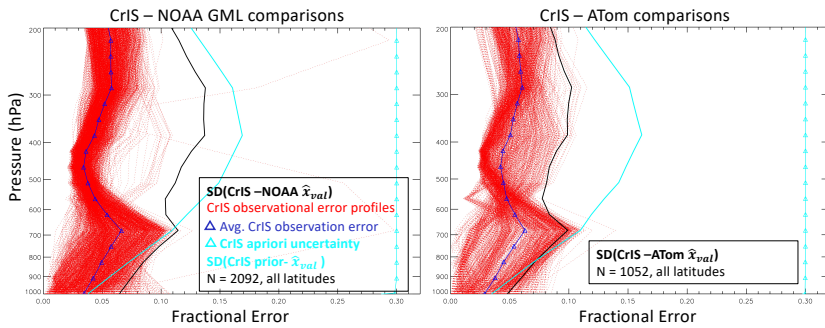
587 Despite the potential for underestimated observational errors, the general behavior of the error
 588 comparison is what we expect from Equation 1, and we can see the retrieval influence on the
 589 shape of SD(CrIS x_{val}). Near the surface, where there is less retrieval sensitivity as indicated
 590 by the averaging kernel, we see that SD(prior x_{val}) becomes smaller than SD(CrIS x_{val}).

Deleted: -
 Deleted: -
 Deleted: -
 Deleted: ,

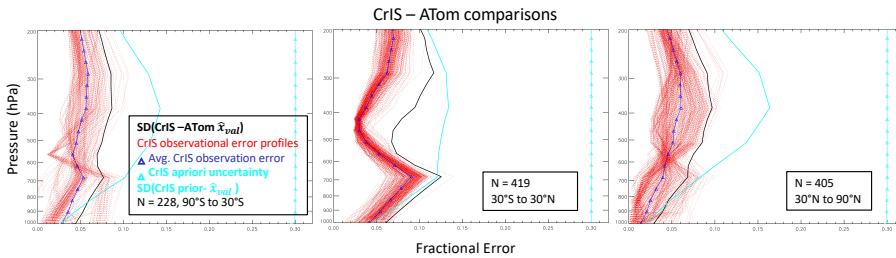
Deleted: for an optimal estimation retrieval
 Deleted: -
 Deleted: -
 Deleted: -

602 This is expected for vertical ranges with less retrieval sensitivity since the priori contribution
 603 becomes more dominant in x_{val} . In contrast, for the middle troposphere where we have the most
 604 sensitivity for TIR remote sensing, it is clear that $SD(CrIS - x_{val})$ represents an improvement
 605 over $SD(prior - x_{val})$. In Figure 12, the error comparison is shown separately for 3 ATom
 606 latitude ranges and we can see that the agreement between observational errors and $SD(CrIS - x_{val})$
 607 x_{val} is closest for ATom flights in the mostly clean middle to high latitude southern hemisphere,
 608 where it is most likely that the aircraft and satellite are observing similar airmasses with
 609 background CO concentrations. These results give confidence that TROPRESS single retrieval
 610 error characterization can be used to weight data for averaging and inverse analysis applications.
 611
 612

Deleted: from Eq. 1
 Deleted: -
 Deleted: -
 Deleted: -



613
 614 **Figure 11.** Error comparison of CrIS observational error estimates and the standard deviation
 615 (SD) of CrIS- x_{val} (in black) for NOAA GML flights in the left panel and ATom flights in the right panel.
 616 Single profile CrIS observational error estimates are plotted in red, with average in dark blue with
 617 triangles. For reference, and the standard deviation of CrIS prior with aircraft x_{val} is in cyan and the
 618 a priori fractional uncertainty (0.3) is shown in cyan with triangles.
 619



620
 621 **Figure 12.** Same as Fig. 11 but for 3 ATom latitude ranges.
 622
 623

624
 625
 626

631 **6. Summary and Conclusions**

632 This study used in situ observations from routine NOAA GML flights and the four ATom
633 campaigns to evaluate TROPES single pixel CO retrievals from the SNPP/CrIS FTS
634 instrument. We find that:

- 635 1) The single FOV CrIS product provides improved representation of CO in smoke plumes
636 compared to retrievals that combine multiple FOVs.
- 637 2) Comparisons with aircraft in situ profiles (after extension, interpolation and application
638 of Eq. 1) show that biases have a vertical dependence in the troposphere that is consistent
639 for both sets of in situ data with average biases that are positive (~ 2.3 %) in the lower
640 troposphere and negative (~ -4.5 %) in the upper troposphere.
- 641 3) Small biases (0.6 % and -0.04 % for NOAA GML and ATom, respectively) are observed
642 for the CrIS CO partial column average VMR corresponding to the aircraft profile
643 vertical ranges.
- 644 4) No significant latitude dependence of CrIS CO column bias is found for the NOAA GML
645 comparisons, but comparisons with ATom, which better covered a range of latitudes,
646 have a slightly more positive bias for tropical scenes that could indicate a small,
647 uncharacterized retrieval dependence on water vapor or another interferent species.
- 648 5) CrIS CO retrievals capture the seasonal and spatial variations observed by ATom.
- 649 6) There is a small negative dependence (magnitude < 0.1 %/ppb) of CrIS bias on CO
650 amount.
- 651 7) Comparisons of computed observational errors and standard deviations of retrieval-
652 aircraft comparison differences show expected vertical behavior and demonstrate
653 significant improvement over the standard deviation of prior-aircraft differences in
654 vertical ranges with higher retrieval sensitivity.

655 TROPES CrIS CO biases detected in this study are in general much smaller than comparison
656 standard deviations. We therefore make no recommendations for automated bias corrections in
657 data processing, similar to other validation studies for satellite CO retrievals (e.g., Deeter et al,
658 2019; 2022). This is unlike other TROPES products such as CH₄ (Kulawik et al., 2021) where a
659 bias correction is more appropriate given the size of bias detected as well as the atmospheric
660 lifetime (~10 years for methane) and reduced atmospheric variability compared to CO. Each
661 analysis using TROPES CrIS CO data must consider the variability of CO over the domain of
662 interest and ascertain whether the biases observed here could affect numerical conclusions. The
663 biases reported from this study will need to be included when long term records of satellite CO
664 observations are harmonized and used together for computing trends, data assimilation or other
665 analyses. For example, with the 22-year record of MOPITT CO profiles, this is especially
666 important when combining datasets since the vertical bias pattern for MOPITT data with respect
667 to in situ observations has a positive bias in the upper troposphere and negative bias in the lower
668 to middle troposphere with the opposite behavior compared to the TROPES/CrIS vertical bias
669 pattern.

670
671 Future validation of the TROPES CrIS CO products will include a longer time record of
672 comparisons and quantification of bias drift, for CrIS on SNPP and on the JPSS satellite series.
673 The validation results presented here demonstrate that these products are suitable for
674 tropospheric CO data analyses. The bias at all vertical levels is <10 % and error characterization

Deleted: the

Deleted: for optimal estimation retrievals

Deleted: .

Deleted:

Deleted:

Deleted:

681 for single retrievals can be used to weight data for averaging and applications such as data
682 assimilation and inverse modelling.

683 *Data availability.* The NOAA GML data were obtained from <https://doi.org/10.7289/V5N58JMF>
684 (Sweeney et al. 2021). The ATom aircraft data were obtained from
685 <https://doi.org/10.3334/ORNDAAC/1581> (Wofsy et al., 2018). TROPES/CrIS CO products
686 are available via the GES DISC from the NASA Tropospheric Ozone and its Precursors from
687 Earth System Sounding (TROPES) project at <https://doi.org/10.5067/11NONOEPXLHS>
688 (Bowman, 2021). The CrIS-aircraft matched data set used here for validation is available from
689 the authors on request.

690 *Author contributions.* HMW, GLF, SSK, JDH, KCP, ML and VHP designed the study and
691 HMW prepared the manuscript. GLF analyzed the satellite/aircraft comparisons and prepared the
692 figures. SSK, KB, DF, VK, ML, KCP, VHP, JRW developed the MUSES algorithm and
693 provided the CrIS CO retrievals. RC and KM participated in the ATom campaign and provided
694 guidance in the use of the measurements. KM provided the NOAA GML aircraft data. All
695 authors reviewed and edited the manuscript.

696
697 *Competing Interests.* Some authors are members of the editorial board of AMT. The peer-review
698 process was guided by an independent editor, and the authors have no other competing interests to
699 declare.

700
701 *Acknowledgements.* This research was conducted at the National Center for Atmospheric Research
702 (NCAR), which is sponsored by the National Science Foundation. Part of this research was carried
703 out at the Jet Propulsion Laboratory (JPL), California Institute of Technology, under a contract
704 with the National Aeronautics and Space Administration. The NOAA GML aircraft observations
705 are supported by NOAA and CIRES. The ATom aircraft data were supported by the NASA
706 Airborne Science Program and Earth Science Project Office. We acknowledge the use of
707 imagery from the NASA Worldview application (<https://worldview.earthdata.nasa.gov/>), part of
708 the NASA Earth Observing System Data and Information System (EOSDIS). We thank Dr.
709 Benjamin Gaubert for his NCAR internal review of the manuscript.

710
711 *Financial support.* The Jet Propulsion Laboratory (JPL), California Institute of Technology, is
712 under a contract with the National Aeronautics and Space Administration (80NM0018D0004).
713 This research has also been supported by NASA via the Tropospheric Ozone and its Precursors
714 from Earth System Sounding (TROPES) project at JPL and a NASA ROSES award:
715 80NSSC18K0687. The NOAA Cooperative Agreement with CIRES is NA17OAR4320101. The
716 NCAR facility is sponsored by the National Science Foundation (grant no. 1852977).

717 718 719 **References**

720
721 Barnet, C (2019), Sounder SIPS: Suomi NPP CrIMSS Level 2 CLIMCAPS Full Spectral Resolution:
722 Atmosphere cloud and surface geophysical state V2, Greenbelt, MD, USA, Goddard Earth Sciences Data
723 and Information Services Center (GES DISC), Last Accessed: [2022.03.23], [10.5067/62SPJFQW5Q9B](https://doi.org/10.5067/62SPJFQW5Q9B)
724

Commented [KM1]: Aircraft network CO data are available in multiple different ObsPacks (https://gml.noaa.gov/ccgg/obspack/data.php?id=obspack_co_1_GLOBALVIEWplus_v2.0_2021-12-08, https://gml.noaa.gov/ccgg/obspack/data.php?id=obspack_multi-species_1_CCGGAircraftFlask_v2.0_2021-02-09). This is the preferred method for obtaining and referencing the data. Also these may be useful for future analyses where you might like to include a larger collection of datasets.

Commented [KM2]: full citation: NOAA Carbon Cycle and Greenhouse Gases Group aircraft-based measurements of CO₂, CH₄, CO, N₂O, H₂ & SF₆ in flask-air samples taken since 1992. C. Sweeney, K. McKain, J. Higgs, S. Wolter, A. Croftwell, D. Neff, E. Dlugokencky, G. Petron, M. Madronich, E. Moglia, M. Croftwell, J. Mund. NOAA Earth System Research Laboratories, Global Monitoring Laboratory. <http://dx.doi.org/10.7289/V5N58JMF>

Deleted: CrIS MUSES

726 Beer, R.: TES on the Aura mission: Scientific objectives, measurements, and analysis overview, *IEEE*
727 *Transactions on Geoscience and Remote Sensing*, vol. 44, no. 5, pp. 1102-1105,
728 doi:10.1109/TGRS.2005.863716, 2006.
729

730 Borsdorff, T., J. Aan de Brugh, H. Hu, I. Aben, O. Hasekamp, and J. Landgraf, Measuring Carbon
731 Monoxide With TROPOMI: First Results and a Comparison With ECMWF-IFS Analysis
732 Data, *Geophysical Research Letters*, 45(6), 28262832, doi:10.1002/2018GL077045, 2018.
733

734 Bourgeois, I., Peischl, J., Thompson, C. R., Aikin, K. C., Campos, T., Clark, H., Commane, R., Daube,
735 B., Diskin, G. W., Elkins, J. W., Gao, R.-S., Gaudel, A., Hints, E. J., Johnson, B. J., Kivi, R., McKain,
736 K., Moore, F. L., Parrish, D. D., Querel, R., Ray, E., Sánchez, R., Sweeney, C., Tarasick, D. W.,
737 Thompson, A. M., Thouret, V., Witte, J. C., Wofsy, S. C., and Ryerson, T. B.: Global-scale distribution of
738 ozone in the remote troposphere from the ATom and HIPPO airborne field missions, *Atmos. Chem.*
739 *Phys.*, 20, 10611–10635, <https://doi.org/10.5194/acp-20-10611-2020>, 2020.
740

741 Bowman, K. W., Rodgers, C. D., Kulawik, S. S., Worden, J., Sarkissian, E., Osterman, G., Steck, T., Lou,
742 M., Eldering, A. and Shephard, M.: Tropospheric emission spectrometer: retrieval method and error
743 analysis, *IEEE Transactions on Geoscience and Remote Sensing*, vol. 44, no. 5, pp. 1297-1307,
744 doi:10.1109/TGRS.2006.871234, 2006.
745

746 Bowman, K. W. et al., TROPRESS Level 2 Algorithm Theoretical Basis Document (ATBD) V1, 2021 at:
747 https://docserver.gesdisc.eosdis.nasa.gov/public/project/TROPRESS/TROPRESS_ATBDv1.1.pdf
748 Last accessed: 2022.04.12
749

750 Bowman, K. W., TROPRESS CrIS-SNPP L2 Carbon Monoxide for West Coast Fires HiRes, Standard
751 Product V1, Greenbelt, MD, USA, Goddard Earth Sciences Data and Information Services Center (GES
752 DISC), Accessed: 2022.02.02, [10.5067/Y3MAIEUNDTBX](https://doi.org/10.5067/Y3MAIEUNDTBX), 2021
753

754 Brasseur, G. P., Hauglustaine, D. A., Walters, S., Rasch, P. J., Muller, J. F., Granier, C., and Tie, X. X.:
755 MOZART, a global chemical transport model for ozone and related chemical trac- ers 1. Model
756 description, *J. Geophys. Res.*, 103, 28265–28289, 1998.
757

758 Buchholz, R. R., Worden, H. M., Park, M., Francis, G. Deeter, M. N., Edwards, D. P., Emmons, L. K.,
759 Gaubert, B., Gille, J., Martinez-Alonso, S., Tang, W., Kumar, R., Drummond, J. R., Clerbaux, C.,
760 George, M., Coheur, P.-F., Hurtmans, D., Bowman, K. W., Luo, M., Payne, V. H., Worden, J. R., Chin,
761 M., Levy, R. C., Warner, J., Wei, Z., Kulawik, S. S.: Air pollution trends measured from Terra: CO and
762 AOD over industrial, fire-prone and background regions, *Remote Sensing of the Environment.*, 256,
763 doi.org/10.1016/j.rse.2020.112275, 2021.
764

765 Byrne, B., Liu, J., Lee, M., Yin, Y., Bowman, K. W., Miyazaki, K., et al.: The Carbon Cycle of
766 Southeast Australia During 2019–2020: Drought, Fires, and Subsequent Recovery. *AGU Advances*,
767 2(4). <https://doi.org/10.1029/2021av000469>, 2021.
768

769 Clerbaux, C., Boynard, A., Clarisse, L., George, M., Hadji-Lazaro, J., Herbin, H., Hurtmans, D.,
770 Pommier, M., Razavi, A., Turquety, S., Wespes, C., and Coheur, P.-F.: Monitoring of atmospheric
771 composition using the thermal infrared IASI/MetOp sounder, *Atmos. Chem. Phys.*, 9, 6041–6054,
772 doi:10.5194/acp-9-6041-2009, 2009.
773

774 Deeter, M. N., D. P. Edwards, J. C. Gille, L. K. Emmons, G. Francis, S.-P. Ho, D. Mao, D. Masters, H.
775 Worden, J. R. Drummond, and P. C. Novelli, The MOPITT version 4 CO product: Algorithm

776 enhancements, validation, and long-term stability, *J. Geophys. Res.-Atmos.*, 115(D7),
777 doi:[10.1029/2009JD013005](https://doi.org/10.1029/2009JD013005), 2010.
778
779 Deeter, M. N., D. P. Edwards, G. L. Francis, J. C. Gille, D. Mao, S. Martinez-Alonso, H. M. Worden, D.
780 Ziskin, and M. O. Andreae, Radiance-based retrieval bias mitigation for the MOPITT instrument: the
781 version 8 product, *Atmos. Meas. Tech.*, 12(8), 4561–4580, doi:[10.5194/amt-12-4561-2019](https://doi.org/10.5194/amt-12-4561-2019), 2019.
782
783 Deeter, M., Francis, G., Gille, J., Mao, D., Martínez-Alonso, S., Worden, H., Ziskin, D., Drummond, J.,
784 Commane, R., Diskin, G., and McKain, K.: The MOPITT Version 9 CO product: sampling enhancements
785 and validation, *Atmos. Meas. Tech.*, 15, 2325–2344, <https://doi.org/10.5194/amt-15-2325-2022>, 2022.
786
787 de Laat, A. T. J., Gloudemans, A. M. S., Schrijver, H., van den Broek, M. M. P., Meirink, J. F., Aben, I.,
788 and Krol, M.: Quantitative analysis of SCIAMACHY carbon monoxide total column measurements,
789 *Geophys. Res. Lett.*, 33, L07807, doi:[10.1029/2005GL025530](https://doi.org/10.1029/2005GL025530), 2006.
790
791 Drummond, J. R., J. Zou, F. Nichitui, J. Kar, R. Deschambaut, and J. Hackett, A review of 9-year
792 performance and operation of the MOPITT instrument, *J. Adv. Space Res.*, doi:[10.1016/j.asr.2009.11.019](https://doi.org/10.1016/j.asr.2009.11.019),
793 2010.
794
795 Edwards, D. P., Emmons, L. K., Hauglustaine, D. A., Chu, A., Gille, J. C., Kaufman, Y. J., Pétron, G.,
796 Yurganov, L. N., Giglio, L., Deeter, M. N., Yudin, V., Ziskin, D. C., Warner, J., Lamarque, J.-F., Francis,
797 G. L., Ho, S. P., Mao, D., Chan, J., and Drummond, J. R.: Observations of Carbon Monoxide and Aerosol
798 From the Terra Satellite: Northern Hemisphere Variability, *J. Geophys. Res.*, 109, D24202,
799 doi:[10.1029/2004JD004727](https://doi.org/10.1029/2004JD004727), 2004.
800
801 Edwards, D. P., Emmons, L. K., Gille, J. C., Chu, A., Attié, J.-L., Giglio, L., Wood, S. W., Haywood, J.,
802 Deeter, M. N., Massie, S. T., Ziskin, D. C., and Drummond, J. R.: Satellite observed pollution from
803 Southern Hemisphere biomass burning, *J. Geophys. Res.*, 111, 14312, doi:[10.1029/2005JD006655](https://doi.org/10.1029/2005JD006655), 2006.
804
805 Eldering, A., S. S. Kulawik, J. Worden, K. Bowman, and G. Osterman, Implementation of cloud
806 retrievals for TES atmospheric retrievals: 2. Characterization of cloud top pressure and effective optical
807 depth retrievals, *J. Geophys. Res.*, 113, D16S37, doi:[10.1029/2007JD008858](https://doi.org/10.1029/2007JD008858), 2008.
808
809 Fu, D., Bowman, K. W., Worden, H. M., Natraj, V., Worden, J. R., Yu, S., Veeckind, P., Aben, I.,
810 Landgraf, J., Strow, L., and Han, Y.: High-resolution tropospheric carbon monoxide profiles retrieved
811 from CrIS and TROPOMI, *Atmos. Meas. Tech.*, 9, 2567–4572579, [https://doi.org/10.5194/amt-9-2567-](https://doi.org/10.5194/amt-9-2567-2016)
812 2016, 2016.
813
814 Fu, D., Kulawik, S. S., Miyazaki, K., Bowman, K. W., Worden, J. R., Eldering, A., Livesey, N. J.,
815 Teixeira, J., Irion, F. W., Herman, R. L., Osterman, G. B., Liu, X., Levelt, P. F., Thompson, A. M., and
816 Luo, M.: Retrievals of tropospheric ozone profiles from the synergism of AIRS and OMI: methodology
817 and validation, *Atmospheric Measurement Techniques*, 11(10), 5587–5605, doi:[10.5194/amt-11-5587-](https://doi.org/10.5194/amt-11-5587-2018-supplement)
818 2018-supplement, 2018.
819
820 Fu D., Millet D.B., Wells K.C., Payne V.H., Yu S., Guenther A., and Eldering A.: Direct retrieval of
821 isoprene from satellite based infrared measurements, *Nature Communication*, 10.3811,
822 doi:[10.1038/s41467-019-11835-0](https://doi.org/10.1038/s41467-019-11835-0). 2019.
823
824 Gambacorta, A., C. Barnett, W. Wolf, T. King, E. Maddy, L. Strow, X. Xiong, N. Nalli, and M. Goldberg
825 An Experiment Using High Spectral Resolution CrIS Measurements for Atmospheric Trace Gases:

826 Carbon Monoxide Retrieval Impact Study, *IEEE Geoscience and Remote Sensing Letters*, 11(9),
827 16391643, doi:10.1109/LGRS.2014.2303641, 2014.
828
829 Gambacorta, A., Nalli, N.R., Barnet, C.D., Tan, C., Iturbide-Sanchez, F., and Zhang, K: *The NOAA*
830 *Unique Combined Atmospheric Processing System (NUCAPS): Algorithm Theoretical Basis Document*
831 *(ATBD)*; ATBD v2.0; NOAA/NESDIS/STAR Joint Polar Satellite System: College Park, MD, USA,
832 2017.
833
834 Gaubert, B., A. F. Arellano, J. Barré, H. M. Worden, L. K. Emmons, S. Tilmes, R. R. Buchholz, F. Vitt,
835 K. Raeder, N. Collins, J. L. Anderson, C. Wiedinmyer, S. Martinez Alonso, D. P. Edwards, M. O.
836 Andreae, J. W. Hannigan, C. Petri, K. Strong, and N. Jones, Toward a chemical reanalysis in a coupled
837 chemistry-climate model: An evaluation of MOPITT CO assimilation and its impact on tropospheric
838 composition, *J. Geophys. Res. Atmos.*, 121(12), 2016JD024863, doi:10.1002/2016JD024863, 2016.
839
840 Gaubert, B., H. M. Worden, A. F. J. Arellano, L. K. Emmons, S. Tilmes, J. Barre, S. M. Alonso, F. Vitt,
841 J. L. Anderson, F. Alkemade, S. Houweling, and D. P. Edwards, Chemical Feedback From Decreasing
842 Carbon Monoxide Emissions, *Geophys. Res. Lett.*, 44(19), 99859995, doi:10.1002/2017GL074987, 2017.
843
844 Gaubert, B., Emmons, L. K., Raeder, K., Tilmes, S., Miyazaki, K., Arellano Jr., A. F., Elguindi, N.,
845 Granier, C., Tang, W., Barré, J., Worden, H. M., Buchholz, R. R., Edwards, D. P., Franke, P., Anderson,
846 J. L., Saunio, M., Schroeder, J., Woo, J.-H., Simpson, I. J., Blake, D. R., Meinardi, S., Wennberg, P. O.,
847 Crounse, J., Teng, A., Kim, M., Dickerson, R. R., He, H., Ren, X., Pusede, S. E., and Diskin, G. S.:
848 Correcting model biases of CO in East Asia: impact on oxidant distributions during KORUS-AQ, *Atmos.*
849 *Chem. Phys.*, 20, 14617–14647, <https://doi.org/10.5194/acp-20-14617-2020>, 2020.
850
851 [George, M., Clerbaux, C., Bouarar, I., Coheur, P.-F., Deeter, M. N., Edwards, D. P., Francis, G., Gille, J.](#)
852 [C., Hadji-Lazaro, J., Hurtmans, D., Inness, A., Mao, D., and Worden, H. M.: An examination of the long-](#)
853 [term CO records from MOPITT and IASI: comparison of retrieval methodology. *Atmos. Meas. Tech.*, 8,](#)
854 [4313–4328, <https://doi.org/10.5194/amt-8-4313-2015>.](#)
855
856 [Gonzalez, Y., Commane, R., Manninen, E., Daube, B. C., Schiferl, L. D., McManus, J. B., McKain, K.,](#)
857 [Hints, E. J., Elkins, J. W., Montzka, S. A., Sweeney, C., Moore, F., Jimenez, J. L., Campuzano Jost, P.,](#)
858 [Ryerson, T. B., Bourgeois, I., Peischl, J., Thompson, C. R., Ray, E., Wennberg, P. O., Crounse, J., Kim,](#)
859 [M., Allen, H. M., Newman, P. A., Stephens, B. B., Apel, E. C., Hornbrook, R. S., Nault, B. A., Morgan,](#)
860 [E., and Wofsy, S. C.: Impact of stratospheric air and surface emissions on tropospheric nitrous oxide](#)
861 [during ATom. *Atmos. Chem. Phys.*, 21, 11113–11132, <https://doi.org/10.5194/acp-21-11113-2021>.](#)
862
863 Hegarty, J., Mao, H., and Talbot, R.: Synoptic influences on springtime tropospheric O₃ and CO over the
864 North American export region observed by TES, *Atmos. Chem. Phys.*, 9, 3755–3776,
865 doi.org/10.5194/acp-9-3755-2009, 2009.
866
867 Hegarty, J., Mao, H., and Talbot, R.: Winter- and summertime continental influences on tropospheric O₃
868 and CO observed by TES over the western North Atlantic Ocean, *Atmos. Chem. Phys.*, 10, 3723–3741,
869 doi.org/10.5194/acp-10-3723-2010, 2010.
870
871 Hegarty, J. D., Cady-Pereira, K. E., Payne, V. H., Kulawik, S. S., Worden, J. R., Kantshev, V., Worden,
872 H. M., McKain, K., Pittman, J. V., Commane, R., Daube Jr., B. C., and Kort, E. A.: Validation and error
873 estimation of AIRS MUSES CO profiles with HIPPO, ATom, and NOAA GML aircraft observations,
874 *Atmos. Meas. Tech.*, 15, 205–223, <https://doi.org/10.5194/amt-15-205-2022>, 2022.
875

Formatted: Font: (Default) Times New Roman, 11 pt, Font color: Text 1

Deleted: ¶

Formatted: Font: (Default) Times New Roman, 11 pt, Font color: Text 1

877 Holloway, T., Levy II, H., Kasibhatla, P., Global distribution of carbon monoxide, *J. Geophys. Res.* 105
878 (D10), 12,123–12,147. <https://doi.org/10.1029/1999JD901173>, 2000.
879
880 Inness, A., M. Ades, A. Agustí-Panareda, J. Barré, A. Benedictow, A.-M. Blechschmidt, J. J. Dominguez,
881 R. Engelen, H. Eskes, J. Flemming, V. Huijnen, L. Jones, Z. Kipling, S. Massart, M. Parrington, V.-H.
882 Peuch, M. Razinger, S. Remy, M. Schulz, and M. Suttie, The CAMS reanalysis of atmospheric
883 composition, *Atmospheric Chemistry and Physics*, 19(6), 35153556, doi:[https://doi.org/10.5194/acp-19-](https://doi.org/10.5194/acp-19-3515-2019)
884 [3515-2019](https://doi.org/10.5194/acp-19-3515-2019), 2019.
885
886 Jiang, Z., Worden, J. R., Worden, H., Deeter, M., Jones, D. B. A., Arellano, A. F., and Henze, D. K.: A
887 15-year record of CO emissions constrained by MOPITT CO observations, *Atmos. Chem. Phys.*, 17,
888 4565–4583, doi.org/10.5194/acp-17-4565-2017, 2017.
889
890 Jones, Dylan B. A., Kevin W. Bowman, Paul I. Palmer, John R. Worden, Daniel J. Jacob, Ross N.
891 Hoffman, Isabelle Bey, and Robert M. Yantosca, Potential of Observations from the Tropospheric
892 Emission Spectrometer to Constrain Continental Sources of Carbon Monoxide, *J. Geophys. Res.* -
893 *Atmospheres*, Vol.108, No. D24, 4789, [10.1029/2003JD003702](https://doi.org/10.1029/2003JD003702), 2003.

894 Juncosa Calahorrano, J. F., Payne, V. H., Kulawik, S., Ford, B., Flocke, F., Campos, T., & Fischer, E. V.
895 Evolution of acyl peroxy nitrates (PANs) in wildfire smoke plumes detected by the Cross-Track Infrared
896 Sounder (CrIS) over the western U.S. during summer 2018. *Geophysical Research Letters*, 48,
897 e2021GL093405. <https://doi.org/10.1029/2021GL093405>, 2021.

898 Karion, A., Sweeney, C., Tans, P., and Newberger, T.: AirCore: An Innovative Atmospheric Sampling
899 System, *Journal Of Atmospheric and Oceanic Technology*, 27, 1839–1853,
900 <https://doi.org/10.1175/2010JTECHA1448.1>, 2010.

901 Kopacz, M., Jacob, D. J., Fisher, J. A., Logan, J. A., Zhang, L., Megretskaia, I. A., Yantosca, R. M.,
902 Singh, K., Henze, D. K., Burrows, J. P., Buchwitz, M., Khlystova, I., McMillan, W. W., Gille, J. C.,
903 Edwards, D. P., Eldering, A., Thouret, V., and Nedelec, P.: Global estimates of CO sources with high
904 resolution by adjoint inversion of multiple satellite datasets (MOPITT, AIRS, SCIAMACHY, TES),
905 *Atmos. Chem. Phys.*, 10, 855–876, <https://doi.org/10.5194/acp-10-855-2010>, 2010.
906
907 Kulawik, S. S., J. Worden, A. Eldering, K. Bowman, M. Gunson, G. B. Osterman, L. Zhang, S. A.
908 Clough, M. W. Shephard, and R. Beer (2006), Implementation of cloud 18 retrievals for Tropospheric
909 Emission Spectrometer (TES) atmospheric retrievals: Part I. Description and characterization of errors on
910 trace gas retrievals, *J. Geophys. Res.*, 111(D24), 2006.

911 Lelieveld, J., Gromov, S., Pozzer, A., Taraborrelli, D., Global tropospheric hydroxyl distribution, budget
912 and reactivity. *Atmos. Chem. Phys.* 16, 12477–12493. <https://doi.org/10.5194/acp-16-12477-2016>, 2016.

913 Liu, J., K. W. Bowman, D. S. Schimel, N. C. Parazoo, Z. Jiang, M. Lee, A. A. Bloom, D. Wunch, C.
914 Frankenberg, Y. Sun, C. W. O'Dell, K. R. Gurney, D. Menemenlis, M. Gierach, D. Crisp, and A.
915 Eldering, Contrasting carbon cycle responses of the tropical continents to the 2015/2016 El
916 Niño, *Science*, 358(6360), eaam5690, doi:[10.1126/science.aam5690](https://doi.org/10.1126/science.aam5690), 2017.
917
918 Martínez-Alonso, S., Deeter, M., Worden, H., Borsdorff, T., Aben, I., Commane, R., Daube, B., Francis,
919 G., George, M., Landgraf, J., Mao, D., McKain, K., and Wofsy, S.: 1.5 years of TROPOMI CO
920 measurements: comparisons to MOPITT and ATom, *Atmos. Meas. Tech.*, 13, 4841–4864,
921 <https://doi.org/10.5194/amt-13-4841-2020>, 2020.

Formatted: Font color: Text 1

Formatted: Font color: Text 1

Formatted: Font color: Text 1

922
 923 Martínez-Alonso, S., Aben, I., Baier, B. C., Borsdorff, T., Deeter, M. N., McKain, K., Sweeney, C., and
 924 Worden, H.: Evaluation of MOPITT and TROPOMI carbon monoxide retrievals using AirCore *in*
 925 *situ* vertical profiles, Atmos. Meas. Tech. Discuss. [preprint], <https://doi.org/10.5194/amt-2022-54>, in
 926 review, 2022.

927
 928 McManus, J. B., Zahniser, M. S., Nelson, D. D., Shorter, J. H., Herndon, S., Wood E., and Wehr, R.:
 929 Application of quantum cascade lasers to high-precision atmospheric trace gas measurements, Opt. Eng.,
 930 49(11), 111124, doi:10.1117/1.3498782, 2010.

931
 932 McMillan, W., Barnet, C., Strow, L., Chahine, M. T., McCourt, M. L., Warner, J. X., Novelli, P. C.,
 933 Korontzi, S., Maddy, E. S., and S. Datta, S: Daily global maps of carbon monoxide from NASA's
 934 Atmospheric Infrared Sounder." Geophysical Research Letters 32, no. 11, 2005.

935
 936 Miyazaki, K., K. Bowman, T. Sekiya, H. Eskes, F. Boersma, H. Worden, N. Livesey, V. H. Payne, K.
 937 Sudo, Y. Kanaya, M. Takigawa, and K. Ogochi, Updated tropospheric chemistry reanalysis and emission
 938 estimates, TCR-2, for 20052018, *Earth System Science Data*, 12(3), 22232259,
 939 doi:<https://doi.org/10.5194/essd-12-2223-2020>, 2020.

940
 941 Moncet, J-L., Uymin, G., Liang, P. and Lipton, A.E: Fast and accurate radiative transfer in the thermal
 942 regime by simultaneous optimal spectral sampling over all channels. Journal of the Atmospheric
 943 Sciences, vol 72, 2622-2641, doi: 0.1175/JAS-D-14-0190.1, 2015.

944
 945 Myhre, G., Shindell, D., Breon, F.-M., Collins, W., Fuglestedt, J., Huang, J., Koch, D., Lamarque, J.-F.,
 946 Lee, D., Mendoza, B., Nakajima, T., Robock, A., Stephens, G., Takemura, T., Zhang, H., Climate Change
 947 2013: The Physical Science Basis. In: Contribution of Working Group I to the Fifth Assessment Report of
 948 the Intergovernmental Panel on Climate Change, chapter Anthropogenic and Natural Radiative Forcing.
 Cambridge University Press, pp. 659–740, 2014.

949 [Nalli, N.R.; Tan, C.; Warner, J.; Divakarla, M.; Gambacorta, A.; Wilson, M.; Zhu, T.; Wang, T.; Wei, Z.;](#)
 950 [Pryor, K.; Kalluri, S.; Zhou, L.; Sweeney, C.; Baier, B.C.; McKain, K.; Wunch, D.; Deutscher, N.M.;](#)
 951 [Hase, F.; Iraci, L.T.; Kivi, R.; Morino, I.; Notholt, J.; Ohyama, H.; Pollard, D.F.; Té, Y.; Velasco, V.A.;](#)
 952 [Warneke, T.; Sussmann, R.; Rettinger, M. Validation of Carbon Trace Gas Profile Retrievals from the](#)
 953 [NOAA-Unique Combined Atmospheric Processing System for the Cross-Track Infrared Sounder. *Remote*](#)
 954 [Sens.](#) **2020**, *12*, 3245. <https://doi.org/10.3390/rs12193245>.

955
 956 Qu, Z., Henze, D. K., Worden, H. M., Jiang, Z., Gaubert, B., Theys, N., & Wang, W.: Sector-based top-
 957 down estimates of NO_x, SO₂, and CO emissions in East Asia. *Geophysical Research Letters*, 49,
 958 e2021GL096009. <https://doi.org/10.1029/2021GL096009>, 2022.

959
 960 Reid, J. S., Koppmann, R., Eck, T. F., and Eleuterio, D. P.: A review of biomass burning emissions part
 961 II: intensive physical properties of biomass burning particles, Atmos. Chem. Phys., 5, 799–825,
 962 <https://doi.org/10.5194/acp-5-799-2005>, 2005.

963
 964 Rodgers, C. D.: Inverse Methods for Atmospheric Sounding, Theory and Practice, World Scientific
 965 Publishing, London, 2000.

966
 967 Rodgers, C. D. and Connor, B. J.: Intercomparison of remote sounding instruments, J. Geophys. Res.,
 968 108, 4116, doi:10.1029/2002jd002299, 2003.

969

Deleted: m

Formatted: Font: (Default) Times New Roman, 11 pt

Formatted: Font: (Default) Times New Roman, 11 pt

Formatted: Font: 11 pt

Formatted: Font: 12 pt, Font color: Auto

Formatted: Space Before: 0 pt, After: 0 pt

971 Santoni, G. W., Daube, B. C., Kort, E. A., Jiménez, R., Park, S., Pittman, J. V., Gottlieb, E., Xiang, B.,
972 Zahniser, M. S., Nelson, D. D., McManus, J. B., Peischl, J., Ryerson, T. B., Holloway, J. S., Andrews, A.
973 E., Sweeney, C., Hall, B., Hints, E. J., Moore, F. L., Elkins, J. W., Hurst, D. F., Stephens, B. B., Bent, J.,
974 and Wofsy, S. C.: Evaluation of the airborne quantum cascade laser spectrometer (QCLS) measurements
975 of the carbon and greenhouse gas suite – CO₂, CH₄, N₂O, and CO – during the CalNex and HIPPO
976 campaigns, *Atmos. Meas. Tech.*, 7, 1509–1526, doi:10.5194/amt-7-1509-2014, 2014.
977
978 Seinfeld, J.H. and Pandis, S.N.: *Atmospheric Chemistry and Physics*. John Wiley and Sons, New York,
979 1998.
980
981 Smith, N., and Barnet, C. D.: CLIMCAPS observing capability for temperature, moisture, and trace gases
982 from AIRS/AMSU and CrIS/ATMS, *Atmos. Meas. Tech.*, 13, 4437–4459, [https://doi.org/10.5194/amt-](https://doi.org/10.5194/amt-13-4437-2020)
983 [13-4437-2020](https://doi.org/10.5194/amt-13-4437-2020), 2020.
984
985 Strobe, S. A., Liu, J., Lait, L., Commane, R., Daube, B., Wofsy, S., Conaty, A., Newman, P., and Prather,
986 M.: Forecasting carbon monoxide on a global scale for the ATom-1 aircraft mission: insights from
987 airborne and satellite observations and modeling, *Atmos. Chem. Phys.*, 18, 10955–10971,
988 <https://doi.org/10.5194/acp-18-10955-2018>, 2018.
989
990 Susskind, J., C. D. Barnet, and J. M. Blaisdell: Retrieval of atmospheric and surface parameters from
991 AIRS/AMSU/HSB data in the presence of clouds, *IEEE Trans. Geosci. Remote Sens.*, 41, 390–409, 2003.
992
993 Suto, H., Kataoka, F., Kikuchi, N., Knuteson, R. O., Butz, A., Haun, M., Buijs, H., Shiomi, K., Imai, H.,
994 and Kuze, A.: Thermal and near-infrared sensor for carbon observation Fourier transform spectrometer-2
995 (TANSO-FTS-2) on the Greenhouse gases Observing SATellite-2 (GOSAT-2) during its first year in
996 orbit, *Atmos. Meas. Tech.*, 14, 2013–2039, <https://doi.org/10.5194/amt-14-2013-2021>, 2021.
997
998 Sweeney, C., Karion, A., Wolter, S., Newberger, T., Guenther, D., Higgs, J. A., Andrews, A. A., Lang, P.
999 M., Neff, D., Dlugokencky, et al.: Seasonal climatology of CO₂ across North America from aircraft
1000 measurements in the NOAA/GML Global Greenhouse Gas Reference Network, *J. Geophys. Res. Atmos.*,
1001 120, 5155–5190, doi:10.1002/2014JD022591, 2015.
1002
1003 Sweeney, C., K. McKain, J. Higgs, S. Wolter, A. Crotwell, D. Neff, E. Dlugokencky, G. Petron, M.
1004 Madronich, E. Moglia, M. Crotwell, J. Mund. NOAA Earth System Research Laboratories, Global
1005 Monitoring Laboratory. NOAA Carbon Cycle and Greenhouse Gases Group aircraft-based measurements
1006 of CO₂, CH₄, CO, N₂O, H₂ & SF₆ in flask-air samples taken since 1992.
1007 <http://dx.doi.org/10.7289/V5N58JMF>, 2021.
1008
1009 Tang, W., Worden, H. M., Deeter, M. N., Edwards, D. P., Emmons, L. K., Martínez-Alonso, S., Gaubert,
1010 B., Buchholz, R. R., Diskin, G. S., Dickerson, R. R., Ren, X., He, H., and Kondo, Y.: Assessing
1011 Measurements of Pollution in the Troposphere (MOPITT) carbon monoxide retrievals over urban versus
1012 non-urban regions, *Atmos. Meas. Tech.*, 13, 1337–1356, <https://doi.org/10.5194/amt-13-1337-2020>,
1013 2020.
1014
1015 Thompson, C. R., Wofsy, S. C., Prather, M. J., Newman, P. A., Hanisco, T. F., Ryerson, T. B., Fahey, D.
1016 W., Apel, E. C., Brock, C. A., Brune, W. H., Froyd, K., Katich, J. M., Nicely, J. M., Peischl, J., Ray, E.,
1017 Veres, P. R., Wang, S., Allen, H. M., Asher, E., Bian, H., Blake, D., Bourgeois, I., Budney, J., Bui, T. P.,
1018 Butler, A., Campuzano-Jost, P., Chang, C., Chin, M., Commane, R., Correa, G., Crounse, J. D., Daube,
1019 B., Dibb, J. E., DiGangi, J. P., Diskin, G. S., Dollner, M., Elkins, J. W., Fiore, A. M., Flynn, C. M., Guo,
1020 H., Hall, S. R., Hannun, R. A., Hills, A., Hints, E. J., Hodzic, A., Hornbrook, R. S., Huey, L. G.,
1021 Jimenez, J. L., Keeling, R. F., Kim, M. J., Kupc, A., Lacey, F., Lait, L. R., Lamarque, J., Liu, J., McKain,

1022 K., Meinardi, S., Miller, D. O., Montzka, S. A., Moore, F. L., Morgan, E. J., Murphy, D. M., Murray, L.
1023 T., Nault, B. A., Neuman, J. A., Nguyen, L., Gonzalez, Y., Rollins, A., Rosenlof, K., Sargent, M., Schill,
1024 G., Schwarz, J. P., Clair, J. M. S., Steenrod, S. D., Stephens, B. B., Strahan, S. E., Strode, S. A., Sweeney,
1025 C., Thames, A. B., Ullmann, K., Wagner, N., Weber, R., Weinzierl, B., Wennberg, P. O., Williamson, C.
1026 J., Wolfe, G. M., & Zeng, L.: The NASA Atmospheric Tomography (ATom) Mission: Imaging the
1027 Chemistry of the Global Atmosphere, *Bulletin of the American Meteorological Society*, 103(3), E761-
1028 E790. <https://journals.ametsoc.org/view/journals/bams/103/3/BAMS-D-20-0315.1.xml>, 2022

1029 Wofsy, S. C., Afshar, S., Allen, H. M., Apel, E. C., Asher, E. C., Barletta, B., Bent, J., Bian, H., Biggs, B.
1030 C., Blake, D. R., Blake, N., Bourgeois, I., Brock, C. A., Brune, W. H., Budney, J. W., Bui, T. P., Butler,
1031 A., Campuzano-Jost, P., Chang, C. S., Chin, M., Commane, R., Correa, G., Crouse, J. D., Cullis, P. D.,
1032 Daube, B. C., Day, D. A., Dean-Day, J. M., Dibb, J. E., DiGangi, J. P., Diskin, G. S., Dollner, M., Elkins,
1033 J. W., Erdesz, F., Fiore, A. M., Flynn, C. M., Froyd, K. D., Gesler, D. W., Hall, S. R., Hanisco, T. F.,
1034 Hannun, R. A., Hills, A. J., Hints, E. J., Hoffman, A., Hornbrook, R. S., Huey, L. G., Hughes, S.,
1035 Jimenez, J. L., Johnson, B. J., Katich, J. M., Keeling, R. F., Kim, M. J., Kupc, A., Lait, L. R., Lamarque,
1036 J.-F., Liu, J., McKain, K., McLaughlin, R. J., Meinardi, S., Miller, D. O., Montzka, S. A., Moore, F. L.,
1037 Morgan, E. J., Murphy, D. M., Murray, L. T., Nault, B. A., Neuman, J. A., Newman, P. A., Nicely, J.
1038 M., Pan, X., Paplawsky, W., Peischl, J., Prather, M. J., Price, D. J., Ray, E., Reeves, J. M., Richardson,
1039 M., Rollins, A. W., Rosenlof, K. H., Ryerson, T. B., Scheuer, E., Schill, G. P., Schroder, J. C., Schwarz,
1040 J. P., St. Clair, J. M., Steenrod, S. D., Stephens, B. B., Strode, S. A., Sweeney, C., Tanner, D., Teng, A.
1041 P., Thames, A. B., Thompson, C. R., Ullmann, K., Veres, P. R., Vieznor, N., Wagner, N. L., Watt, A.,
1042 Weber, R., Weinzierl, B., Wennberg, P. O., Williamson, C. J., Wilson, J. C., Wolfe, G. M., Woods, C. T.,
1043 and Zeng, L. H.: ATom: Merged Atmospheric Chemistry, Trace Gases, and Aerosols, ORNL DAAC
1044 [data set], Oak Ridge, TN, USA, <https://doi.org/10.3334/ORNLDAAC/1581>, 2018.

1045 Worden, H. M., J. Logan, J. R. Worden, R. Beer, K. Bowman, S. A. Clough, A. Eldering, B. Fisher, M.
1046 R. Gunson, R. L. Herman, S. S. Kulawik, M. C. Lampel, M. Luo, I. A. Megretskaja, G. B. Osterman, M.
1047 W. Shephard, Comparisons of Tropospheric Emission Spectrometer (TES) ozone profiles to ozonesodes:
1048 methods and initial results, *J. Geophys. Res.*, 112, D03309, [doi:10.1029/2006JD007258](https://doi.org/10.1029/2006JD007258), 2007.

1049 Worden, H. M., Deeter, M. N., Frankenberg, C., George, M., Nichitiu, F., Worden, J., Aben, I., Bowman,
1050 K. W., Clerbaux, C., Coheur, P. F., de Laat, A. T. J., Detweiler, R., Drummond, J. R., Edwards, D. P.,
1051 Gille, J. C., Hurtmans, D., Luo, M., Martínez-Alonso, S., Massie, S., Pfister, G., and Warner, J. X.:
1052 Decadal record of satellite carbon monoxide observations, *Atmos. Chem. Phys.*, 13, 837–850,
1053 <https://doi.org/10.5194/acp-13-837-2013>, 2013.

1054 Zheng, B., Chevallier, F., Yin, Y., Ciais, P., Fortems-Cheiney, A., Deeter, M. N., Parker, R. J., Wang, Y.,
1055 Worden, H. M., and Zhao Y.: Global atmospheric carbon monoxide budget 2000–2017 inferred from
1056 multi-species atmospheric inversions: *Earth Syst. Sci. Data*, 11, 1411–1436, [doi.org/10.5194/essd-11-](https://doi.org/10.5194/essd-11-1411-2019)
1057 1411-2019, 2019.

Formatted: Font color: Text 1

Formatted: Font color: Text 1

Formatted: Font color: Text 1